November 2016

X-Ray Characterization of Mesophases and Phase Transitions of DNA Analogues in Solutions

Mustafa SELCUK Yasar

X-RAY CHARACTERIZATION OF MESOPHASES AND PHASE TRANSITIONS OF DNA ANALOGUES IN SOLUTIONS

A Dissertation Presented

by

MUSTAFA SELCUK YASAR

Submitted to the Graduate School of the
University of Massachusetts Amherst in partial fulfillment
of the requirements for the degree of

DOCTOR OF PHILOSOPHY

September 2016

Department of Physics

X-RAY CHARACTERIZATION OF MESOPHASES AND PHASE TRANSITIONS OF DNA ANALOGUES IN SOLUTIONS

A Dissertation Presented

by

MUSTAFA SELCUK YASAR

Approved as to style and content by:

Adrian Parsegian, Chair

Rudolf Podgornik, Member

Anthony Dinsmore, Member

Murugappan Muthukumar, Member

Rory Miskimen, Department Chair
Department of Physics

ABSTRACT

X-RAY CHARACTERIZATION OF MESOPHASES AND PHASE TRANSITIONS OF DNA ANALOGUES IN SOLUTIONS

SEPTEMBER 2016

MUSTAFA SELCUK YASAR

B.Sc., KOÇ UNIVERSITY

Ph.D., UNIVERSITY OF MASSACHUSETTS AMHERST

Directed by: Professor Adrian Parsegian

We think of DNA as double-stranded helices (duplex), but the polymer exists in many conformations. Several triplex and quadruplex DNA structures can be formed in laboratory settings and exist in nature. This thesis first provides a brief description of the nature of the order in arrays of duplex DNA under biologically relevant molecular crowding conditions. Then we compare the duplex DNA mesophases with the corresponding liquid crystalline phase behavior of the triplex and quadruplex DNA analogues. In particular, we focus on G-quadruplexes.

Observed in the folds of guanine-rich oligonucleotides, G-quadruplex structures are based on G-quartets formed by hydrogen bonding and cation-coordination of guanosines. In dilute 5′-guanosine monophosphate (GMP) solutions, G-quartets form by the self-assembly of four GMP nucleotides. We use x-ray diffraction to characterize the columnar liquid-crystalline mesophases in concentrated solutions of var-

ious model G-quadruplexes. We then probe the transitions between mesophases by varying the PEG solution osmotic pressure, thus mimicking *in vivo* molecular crowding conditions. Using the *GMP-quadruplex*, built by the stacking of G-quartets with no covalent linking between them, as the baseline, we report the liquid-crystalline phase behaviors of two other related G-quadruplexes: (i) the intramolecular parallel-stranded G-quadruplex formed by the 22-mer four-repeat human telomeric sequence $AG_3\big(TTAG_3\big)_3$ and (ii) the intermolecular parallel-stranded G-quadruplex formed by the TG_4T oligonucleotides. Finally, we compare the mesophases of the G-quadruplexes, under PEG-induced crowding conditions, with the corresponding mesophases of the canonical duplex and triplex DNA analogues.

The mesophase transitions of higher-order DNA structures, i.e., triplexes and quadruplexes, have nature and features similar to the *cholesteric−hexatic transition* of duplex DNA. We explore the sensitivity of the DNA mesophase transitions (including the DNA density change at the transition) to thermodynamic variables such as osmotic pressure, ionic strength, and temperature. Measurements of the mesophase transitions of DNA analogues reveal relations between high-density DNA packing and the helical and elastic characteristics of the DNA structures.

CONTENTS

LIST OF TABLES

Table **Page**

LIST OF FIGURES

Figure **Page**

INTRODUCTION

This thesis presents a study of the cholesteric-to-hexatic phase transition of duplex DNA as well as the mesophase transitions (having nature and features similar to the cholesteric−hexatic transition) of DNA analogues, i.e., triplexes and quadruplexes [1–4]. First, it describes our measurements of the osmotic-pressure and ionic-strength dependence of the duplex DNA density in two mesophases: cholesteric and hexatic [5, 6]. We include a detailed description of the transition between the two phases. While the DNA *cholesteric−hexatic transition* has been observed before, it has remained unclear whether the transition is first-order or second-order.

In this work, DNA arrays are equilibrated in polyethylene glycol (PEG) solutions to produce the osmotic pressures, and the packing density is measured by x-ray diffraction [7]. We explore the sensitivity of the transitions (including the DNA density change at the transition) to thermodynamic variables such as osmotic pressure, ionic strength, and temperature. We try to express an understanding of how DNA analogues are organized in response to thermodynamic variables.

We first focus on the basic physical principles of the organization and packing of DNA chains. In Chapter 1 we review the parameterization of the forces governing DNA-DNA interactions. We introduce the mathematical forms of the *bare interaction* osmotic pressures, predicted to compare with hydrostatic pressure curves (i.e., applied external pressure vs. DNA-chain interaxial distances). We also present preliminary analysis and fittings of the duplex DNA hexatic-phase data. Additionally, we introduce an empirical *fluctuational free energy* and present duplex DNA cholesteric-phase data analysis. The radial *density fluctuations* (related to DNA-*chain fluctuations*) are pronounced in the cholesteric phase.

In Chapter 2 we introduce the DNA analogues (triplex and G-quadruplex DNA) considered in this thesis and describe their mesophase behaviors. The changes observed in the x-ray diffraction patterns at the mesophase transitions of the duplex, triplex, and G-quadruplex are essentially similar. At these transitions, both the intra- and the intercolumnar order change significantly and abruptly. We discuss the liquid-crystalline phase behaviors of the DNA analogues with or without sugar-phosphate backbones and with different numbers of bases contributing to the stacking units (i.e., base-pair for duplex, base-triplet for triplex, and G-quartet for G-quadruplex).

Chapter 3 starts with an overview of the nature of the condensation transition of DNA as seen by x-ray diffraction. We then introduce the *thermodynamic potentials* of the phase transitions and present thermodynamic analysis of the data. In particular, the sensitivity of the transition free energy (i.e., free-energy changes at the transition) to temperature allows computation of the change in packing entropy at the transition. We use the Clausius-Clapeyron relation and calculate the entropy in the *less-ordered fluctuating phases* of duplex and G-quadruplex DNA. Information about the entropy of cholesteric packing can also be obtained by further analysis of the x-ray diffraction peak widths, as discussed in Chapter 4. Much broader x-ray diffraction peaks for *GMP-quadruplexes* than for duplexes in the less-ordered fluctuating phase indicate strong entropic contributions from chain fluctuations. Furthermore, in Chapter 4 we discuss possible mechanisms for the reduction of repulsive interactions at the DNA mesophase transitions.

CHAPTER 1

FUNDAMENTAL INTERACTIONS IN THE DNA PACKING

1.1 Introduction

Ever since its discovery, the nature of the cholesteric−hexatic transition of long-fragment (few microns long) duplex DNA has remained unclear [6]. The transition was presumed to be either continuous second-order or weak first-order with a small volume discontinuity. The available accuracy of the osmotic pressures did not permit definitive resolution of the transition [8, 9]. However, by accurate control of the osmotic pressure via its known temperature dependence [10], we have been able to confirm a phase-coexistence region of width $\sim$2Å interaxial spacing. The existence of a *first-order transition* in monovalent salt solutions suggests a *universal* mechanism by which strong repulsive interactions at high densities are attenuated by structural re-arrangements [11] of DNA helices. This effect is distinct from that of *polyvalent-counterion-induced* reduction of DNA-DNA repulsive interactions [12–15]. In addition, *counterion binding* and *charge neutralization* must be included to account for the salt dependence of the transition properties.

Phase coexistence and an abrupt density change at finite osmotic pressures have been observed only for DNA solutions containing polyvalent counterions [8] such as cobalt hexammine $\left(\mathrm{CoHex}^{3+}\right)$ at concentrations below a critical value (the *upper critical concentration*) that induces immediate precipitation of the DNA. When the polyvalent salt is below the upper critical concentration, precipitation does not occur spontaneously, but precipitation can be induced by an additional osmotic pressure that pushes the DNA through a first-order expanded $\rightarrow$ condensed transition.

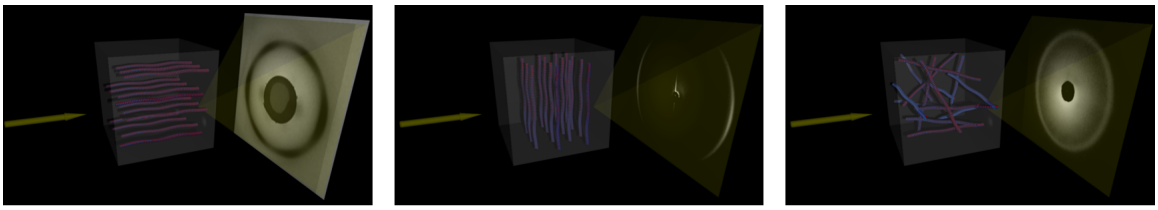

(a) (b) (c)

Figure 1.1. Typical x-ray images of oriented DNA bundles in the hexatic phase with DNA helical axis (a) parallel and (b) perpendicular to the x-ray beam. The sixfold symmetry in (a) shows the long-range bond orientational order in the hexatic phase, where DNA chains are packed in a parallel straight arrangement. This symmetry does not exist in x-ray images of DNA samples in the cholesteric phase (c), which gives a liquid-like circular diffraction pattern.

The *condensation transition* of duplex DNA (i.e., collapse into an ordered aggregate induced by osmotic pressure) was thought to occur only at polyvalent counterion concentrations above a finite value (the *lower critical concentration*) [8, 14]. We now know [10] that the osmotic-pressure-induced DNA condensation transition occurs for all [$CoHex^{3+}$], from 0 to its upper critical concentration. Addition of polyvalent counterions at subcritical concentrations increases the abrupt volume change that is already present at the cholesteric−hexatic transition in NaCl solutions. These facts point to a *continuity of states* [10] between the cholesteric−hexatic transition of DNA in monovalent-salt solutions and the DNA condensation transition, frequently viewed as entirely distinct phenomena [8, 14]. These transitions are indeed similar even in terms of an identical diffraction fingerprint (Fig. 1.1 and Fig. 1.2.)

It is now clear that the cholesteric−hexatic transition is a first-order transition with abrupt changes in the DNA *positional order* and density. Positional disorder is related to radial density fluctuations, as seen in the cholesteric phase by a broader x-ray radial intensity peak (i.e., a Gaussian shape around the average radial momentum transfer). On the other hand, the Lorentzian peak shape in the hexatic phase is evidence of *long-range* positional order, which for duplex DNA decays exponentially

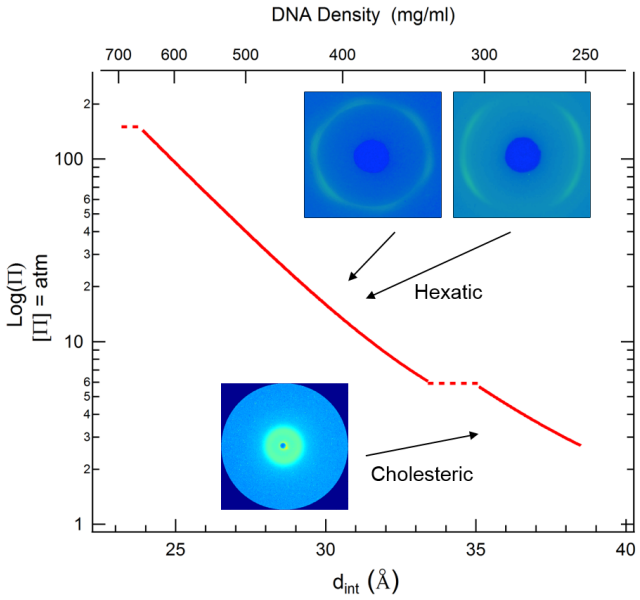

Figure 1.2. Osmotic pressure dependence of the interaxial spacing (lower horizontal axis) and DNA density (upper horizontal axis) for duplex DNA array in the presence of 0.4 M NaCl. The curves are obtained from polynomial fits to osmotic stress raw data. Horizontal dashed line represents the first-order cholesteric-to-hexatic transition with increasing DNA density. At high density (or osmotic pressure) there is also an hexatic-to-orthorhombic transition. The images indicate the scattering intensity footprints of different phases (see Fig. 1.1).

with a characteristic length (*correlation length*) on the order of 5-to-6 neighbor separations. For G-quadruplexes (see Chapter 2) the correlation length in the ordered phase is 9-to-10 neighbor separations and is independent of osmotic pressure (or of DNA density).

We also see x-ray diffraction evidence for *azimuthal orientation* of chains in the DNA fiber [16,17] at hexatic and condensed packing densities, indicating that helical interactions [11,18] are pronounced in the hexatic and condensed phases. In addition, the *bond-orientational order* [19,20] is *macroscopic* in the hexatic phase, leading to the appearance of a sixfold azimuthal symmetry in the x-ray diffraction pattern when the chains are aligned parallel to the x-ray beam (Fig. 1.1). This symmetry occurs concurrently with the abrupt density change at the transition. Previous authors

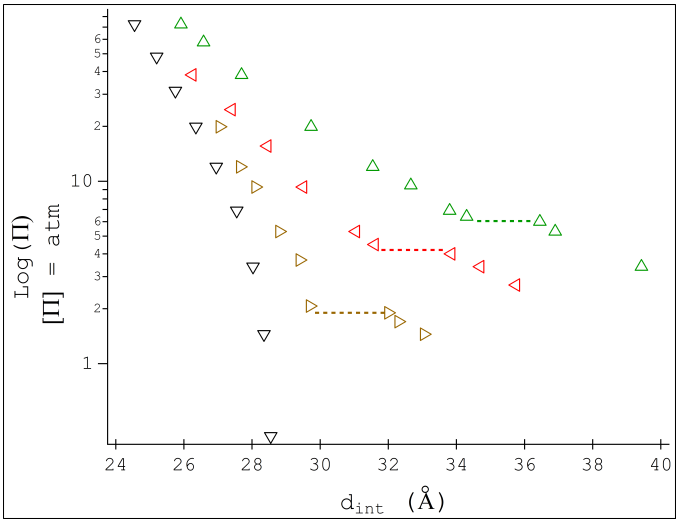

Figure 1.3. Osmotic pressure induced transitions for different [CoHex] at [NaCl]=0.3M. Green triangles: [CoHex]=0. Black inverted triangles: [CoHex]=[CoHex]*=28mM. Red left-facing triangles: [CoHex]=3mM. Brown right-facing triangles: [CoHex]=12mM. Horizontal broken lines show the cholesteric−hexatic transitions. For [CoHex]=3mM and [CoHex]=12mM, data are shown up to the pressure where d_{int} is approximately 0.1Å larger than the interaxial distance measured when [CoHex]=[CoHex]*; above that they superimpose with the [CoHex]* data.

[6] could not definitively address the question of whether this change is continuous. The broadening of the x-ray diffraction radial intensity peak with increasing DNA density [21] (seen in the hexatic phase of duplex DNA) is explained by distortions of the bond-orientational order and hexatic packing due to azimuthal angle-dependent interactions [20]. This effect is not pronounced in the high-density packings of G-quadruplexes, indicating that helical interactions and alignment of four-strand DNA structures (made of four equally spaced phosphate strands) permit tighter packing without bond-angle distortions (see Chapter 2).

Continuity of states between the cholesteric−hexatic transition and the condensation transition in DNA solutions: The order of the cholesteric−hexatic transition is relevant also for the DNA condensation transition induced by osmotic pressure at subcritical [$CoHex^{3+}$]. The cholesteric-to-hexatic transition exists at

any $[CoHex^{3+}] < [CoHex^{3+}]^*$, where $[CoHex^{3+}]^*$ is the upper critical concentration. We find that $[CoHex^{3+}]^*$=28mM in [NaCl]=0.3M solutions. The osmotic pressure-induced transitions for different $[CoHex^{3+}]$ are shown in Fig. 1.3. With increasing $[CoHex^{3+}]$, Π_{tr} decreases without a significant change in the volume discontinuity at the transition.

1.2 Parametrization of the bare interactions

Two significant observations about interactions in the hexatic phase of duplex DNA in monovalent-salt solutions, based on our osmotic pressure data, are as follows: In the hexatic phase at low DNA densities near the hexatic-to-cholesteric transition,
(i) the ionic-strength dependence of the DNA density (at a fixed pressure) is very pronounced, and
(ii) the apparent decay length from the osmotic pressure data (see Fig. 1.8) is close to the Debye length.
These results suggest that with decreasing DNA density in the hexatic phase, electrostatic interactions dominate.

When the highly charged DNA molecule is placed in an electrolyte solution and ions are structured around it, the first layer of this structuring will be formed mostly by positively charged ions. In the case of strong direct interactions (i.e., adsorption or binding) between the first layer of structured ions and the phosphate residues on the DNA surface, the *net charge* of the molecule will be smaller than its *bare charge*. The strength of the ion-phosphate interactions depends on the type and valence of the ions. Comparison of the measured DNA osmotic-pressure curves with the forms predicted using linearized mean-field Poisson-Boltzmann theory is unreliable without knowing the net charge of the molecule because of the following:
When the surface-to-surface separation between the molecules is smaller than about 1 nm, DNA osmotic-pressure curves for all ionic concentrations converge to a single

curve suggesting a universal short-range repulsion that is independent of ionic strength (Fig. 1.8). Therefore, one of our tasks is to decompose the interactions (in the hexatic phase) into two parts having different magnitudes and decay lengths. This can be done more accurately using an *effective* surface charge for the DNA molecule predicted by thermodynamic analysis of the data (see Chapter 3).

1.2.1 Potential of cylindrical surfaces

The general solution of the Poisson-Boltzmann equation for the electrostatic potential of a uniformly charged infinitely long cylinder is azimuthally symmetric, varying only as the distance r from the cylinder axis. In a linearized mean-field approximation, the dependence of this potential on r can be described with modified Bessel functions of the first and second kinds of order zero, i.e., $I_0(x)$ and $K_0(x)$, respectively. The argument x is the ratio of r to a characteristic length λ (the Debye screening length) that is related to the solution permittivity, temperature, and bulk concentrations of the mobile ions.

The electrostatic potential of a helical "chain" molecule can be approximated by the Poisson-Boltzmann cylindrical solution at distances large enough from the molecular axis that the helicity of the molecule does not play a role. Helical structure is expected [11] to be important [16] at distances where r is comparable to or less than the helical pitch length (the axial distance per helical turn). The solution of the Poisson-Boltzmann equation for helical molecules is presented in the Kornyshev-Leikin theory of helix-specific interactions [11]. We explain the dependence of the electrostatic potential of chain molecules on their helicities in Subsection 1.2.3. First we consider cylinder-cylinder interactions and explain (i) the potential of a uniformly charged cylinder, (ii) the osmotic pressure of a hexagonal array of cylinders. In Subsection 1.2.2, we use a cylindrical cell model [22] to derive (ii) from (i).

The characteristic length used to describe the radial decay of electrostatic potentials of uniformly charged smooth surfaces in electrolyte solutions is called the *Debye length*, after Dutch physicist Peter Debye [23]. For monovalent salt solutions at room temperature (where the dielectric permittivity of water is approximately 80 times larger than the vacuum permittivity), the approximate expression for the Debye length is

$$\lambda_D = \frac{3.05\text{Å}}{\sqrt{I(M)}} \tag{1.1}$$

where $I(M)$ is the molar ionic strength (which is equal to the molar ionic concentration for monovalent salts).

DNA is a highly charged molecule, made of nucleotides having one net negative elementary charge each. When DNA is in its double-strand form (duplex DNA), the repeating unit is a pair of nucleotides, the *base-pair*. When fully hydrated, duplex DNA is said to be in the "B-form," where the charged groups (i.e., the phosphates of the two nucleotides in the base pair) are near the molecular surface. The *bare charge* of the B-form of duplex DNA (i.e., when it is fully charged) can be defined via an *effective* surface-charge density,

$$\sigma = \frac{e}{\pi a b} \tag{1.2}$$

where e is the magnitude of the elementary charge, a≈10Å is the B-DNA radius, and b≈3.4Å is the axial distance per base pair.

The electrostatic potential of a cylinder, $\Phi(r)=AK_0(r/\lambda_D)+BI_0(r/\lambda_D)$, is the solution of a modified Bessel differential equation, where A and B are undefined constants evaluated from the boundary conditions. For an isolated cylinder, one of the boundary conditions is $\Phi(r)=0$ at $r=\infty$. The function $K_0(x) \to 0$ when $x \to \infty$; therefore the boundary condition at $r=\infty$ is satisfied when $B=0$ and $\Phi(r)=AK_0(r/\lambda_D)$. Applying Gauss's Law, the boundary condition on the cylinder surface is

$$\left(\frac{\partial \Phi}{\partial r}\right)_{r=a} = -\frac{\sigma}{\epsilon\epsilon_0} \tag{1.3}$$

where $\epsilon\epsilon_0$ is the dielectric permittivity of the medium (ϵ_0 is vacuum permittivity and $\epsilon \approx 80$ for water). Using the identity

$$\frac{dK_0(x)}{dx} = -K_1(x) \tag{1.4}$$

yields

$$A = \frac{\sigma}{\epsilon\epsilon_0} \frac{\lambda_D}{K_1(a/\lambda_D)} \ , \tag{1.5}$$

relating the potential to surface charge density and dielectric permittivity. The electrostatic potential of an isolated cylinder is then

$$\Phi(r) = \frac{\sigma\lambda_D}{\epsilon\epsilon_0} \frac{K_0(r/\lambda_D)}{K_1(a/\lambda_D)} \ . \tag{1.6}$$

1.2.2 Cylindrical cell model and osmotic pressure

In a hexagonal array of long cylindrical molecules, the hexagonal cross-sectional area surrounding each molecule can be approximated by a circle of the same area known as the *Wigner-Seitz cell* [22]. The radius R of this cell is found by constructing a *Voronoi cell* around each molecule, calculating its cross-sectional area, equating this to πR^2, and solving for R. The result is:

$$R = \left(\frac{\sqrt{3}}{2\pi}\right)^{\frac{1}{2}} d_{int} \simeq 0.525 \ d_{int} \simeq 1.05 \ \frac{d_{int}}{2} \tag{1.7}$$

where d_{int} is the interaxial distance, or the center-to-center separation, between nearest-neighbor molecules in the 2D hexagonal array.

The Wigner-Seitz cell osmotic pressure Π_{cell} is locally balanced by the osmotic pressures of the neighboring cells. The external pressure Π_{ext} provided by the external PEG solution compresses the whole array and holds the molecules together against their internal cell pressure. The osmotic pressure at the cell wall, where the electric

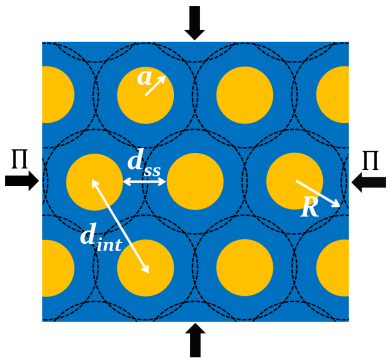

Figure 1.4. Cylindrical cell model: Black circles are the Wigner-Seitz cell boundaries when the cell radius is $R = 1.05(d_{int}/2)$.

field is zero by symmetry, can be formulated using van't Hoff's law. In the presence of monovalent salt only,

$$\Pi_{cell}(R) = k_B \mathrm{T}\Big[n_+(R) + n_-(R) - 2n_\infty\Big] \tag{1.8}$$

where, $n_+(R)$ and $n_-(R)$ are number densities of the positive and negative ions at the cell boundary and n_∞ is the ion number density in the reservoir, where $n_+ = n_- = n_\infty$ (due to electroneutrality of the reservoir). In the *mean-field approximation*, the electrostatic energies of the mobile ions, relative to those in the reservoir, are described in terms of the electrostatic potential which, for reasons to become clear later, we now call $\Phi_e(r)$. For monovalent salts, the electrostatic potential energies of the cations and anions are $\pm e\Phi_e(r)$ respectively.

The dependence of the ion number densities at the cell boundary on the cell radius R can be described via the *Boltzmann distribution*,

$$n_\pm(R) = n_\infty e^{\mp \frac{e\Phi_e(R)}{k_B \mathrm{T}}}\ , \tag{1.9}$$

which, using Eq. 1.8, yields

$$\Pi_{cell,e}(R) = k_B \mathrm{T} n_\infty \left(e^{-\frac{e\Phi_e(R)}{k_B \mathrm{T}}} + e^{+\frac{e\Phi_e(R)}{k_B \mathrm{T}}} - 2 \right) . \tag{1.10}$$

For $e\Phi_e << $ thermal energy $k_B\mathrm{T}$,

$$e^{\pm\frac{e\Phi_e(R)}{k_B \mathrm{T}}} \approx 1 \pm \frac{e\Phi_e(R)}{k_B \mathrm{T}} + \frac{1}{2}\left(\frac{e\Phi_e(R)}{k_B \mathrm{T}} \right)^2 \tag{1.11}$$

yields $\Pi_{cell,e}(R)$ in the *Debye-Hückel approximation* as

$$\Pi_{cell,e}(R) = k_B \mathrm{T} n_\infty \left(\frac{e\Phi_e(R)}{k_B \mathrm{T}} \right)^2 . \tag{1.12}$$

Using

$$\kappa_e^2 = \frac{2e^2 n_\infty}{\epsilon\epsilon_0 k_B \mathrm{T}} = 8\pi l_B n_\infty ,$$

where κ_e=λ_D^{-1} is called the Debye-Hückel constant, and l_B is the *Bjerrum length*,

$$l_B = \frac{e^2}{4\pi\epsilon\epsilon_0 k_B \mathrm{T}} ,$$

Eq. 1.12 yields

$$\Pi_{cell,e}(R) \approx \frac{\kappa_e^2 \epsilon\epsilon_0}{2} \Phi_e^2(R) . \tag{1.13}$$

The electrostatic potential of an isolated charged cylinder (i.e., for $\Phi_e(r) = 0$ at $r = \infty$) is described in the previous section (Eq. 1.6) as

$$\Phi_e(r) = \frac{\sigma}{\epsilon\epsilon_0} \frac{1}{\kappa_e} \frac{K_0(\kappa_e r)}{K_1(\kappa_e a)} . \tag{1.14}$$

Unlike the case of an isolated cylinder, in a hexagonal array of charged cylinders, the proper boundary condition on the Wigner-Seitz cell surface is

$$\left(\frac{\partial \Phi}{\partial r} \right)_{r=R} = 0 . \tag{1.15}$$

Applying 1.15 and the boundary condition at the cylinder surface (Eq. 1.3) to the general solution,

$$\Phi(r) = AK_0(\kappa_e r) + BI_0(\kappa_e r) \ , \tag{1.16}$$

and by use of Eq. 1.4 and the identity

$$\frac{dI_0(x)}{dx} = I_1(x) \ , \tag{1.17}$$

we obtain (see Appendix)

$$\Phi_e(r) = \frac{\sigma}{\epsilon\epsilon_0}\frac{1}{\kappa_e}\left[\frac{I_1(\kappa_e R)K_0(\kappa_e r) + K_1(\kappa_e R)I_0(\kappa_e r)}{I_1(\kappa_e R)K_1(\kappa_e a) - K_1(\kappa_e R)I_1(\kappa_e a)}\right] . \tag{1.18}$$

Combining Eqs. 1.13 and 1.18, we find

$$\Pi_{cell,e}(R) = \frac{\sigma^2}{2\epsilon\epsilon_0}\left[\frac{I_1(\kappa_e R)K_0(\kappa_e R) + K_1(\kappa_e R)I_0(\kappa_e R)}{I_1(\kappa_e R)K_1(\kappa_e a) - K_1(\kappa_e R)I_1(\kappa_e a)}\right]^2 . \tag{1.19}$$

In terms of the factor

$$\alpha(\kappa_e R, \kappa_e a) = \frac{1}{2}\left[\frac{1 + \dfrac{K_1(\kappa_e R)I_0(\kappa_e R)}{I_1(\kappa_e R)K_0(\kappa_e R)}}{1 - \dfrac{K_1(\kappa_e R)I_1(\kappa_e a)}{I_1(\kappa_e R)K_1(\kappa_e a)}}\right] \tag{1.20}$$

Eq. 1.19 can be expressed as

$$\Pi_{cell,e}(R) = \left[\alpha^2(\kappa_e R, \kappa_e a)\ \frac{\sigma^2}{\epsilon\epsilon_0}\right]\left[\frac{K_0(\kappa_e R)}{K_1(\kappa_e a)}\right]^2 . \tag{1.21}$$

The dependence of the factor α on R (for different κ_e when a=10Å) is shown in Fig. 1.5. Over the range of R where the electrostatic effects dominate and the cholesteric−hexatic transitions take place, α varies from ≈1.3 to ≈1.5 for the monovalent salt concentrations used in this study. We ignore this effect and assume α as

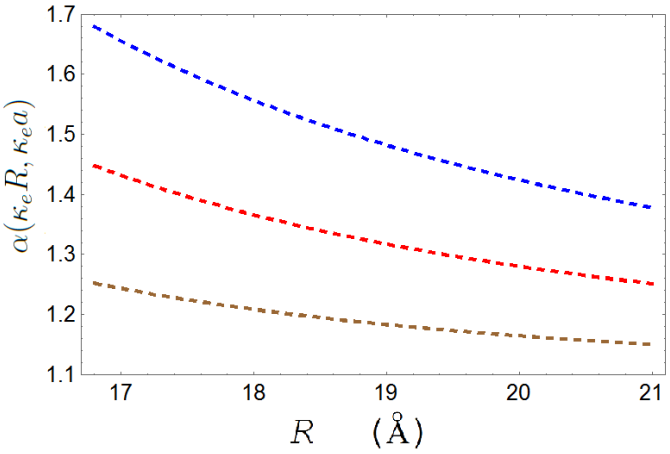

Figure 1.5. Dependence of α on Wigner-Seitz cell radius R for a=10Å and κ_e=(9Å)$^{-1}$, (7Å)$^{-1}$, (5Å)$^{-1}$ from top to bottom, respectively.

a correction factor, which is independent of the ionic strength (an approximation we discuss later). Therefore

$$\Pi_{cell,e}(R) \approx \alpha^2 \frac{\sigma^2}{\epsilon\epsilon_0} \left[\frac{K_0(\kappa_e R)}{K_1(\kappa_e a)} \right]^2 . \tag{1.22}$$

When the dependence of α and σ on the cell radius R is ignored,

$$\Pi_{cell,e}(R) \approx \tilde{\Pi}_e \left[\frac{K_0(\kappa_e R)}{K_1(\kappa_e a)} \right]^2 , \tag{1.23}$$

where

$$\tilde{\Pi}_e \equiv \frac{\alpha^2 \sigma^2}{\epsilon\epsilon_0} \tag{1.24}$$

is a constant prefactor relating the magnitude of the electrostatic osmotic pressure to the solution dielectric permittivity $\epsilon\epsilon_0$, the unknown cylinder surface-charge density σ, and the factor α.

Osmotic pressure due to water structuring in the cell (related to the free-energy change of water molecules when they are near the cylinder surface) can be described with the same formalism (discussed in Section 1.3),

$$\Pi_{cell,h}(R) = \tilde{\Pi}_h \left[\frac{K_0(\kappa_h R)}{K_1(\kappa_h a)} \right]^2, \tag{1.25}$$

where $\tilde{\Pi}_h$ and κ_h are parameters related to the magnitude and radial decay of a *phenomenological hydration potential* [25] describing water structuring. Finally, the PEG-imposed external osmotic pressure Π_{ext} (holding the hexagonal array of molecules together at a density of one chain per Wigner-Seitz cell of radius R) is equal to the total internal osmotic pressure on the cell wall,

$$\Pi_{ext}(R) = \Pi_{cell}(R) = \Pi_{cell,e}(R) + \Pi_{cell,h}(R) \ .$$

1.2.3 Helix specific interactions

In the condensed phase the "chains" are stiff and parallel. There is also evidence that the chains are *azimuthally oriented*. That is to say that the molecular surface-charge density varies with the azimuthal angle ϕ around the long axis. This occurs when chain motions are suppressed and the interaction potentials also vary azimuthally. The solution of the linearized Poisson-Boltzmann equation,

$$\nabla^2 \Phi(\vec{r}) - \kappa^2 \Phi(\vec{r}) = -\frac{\rho_{fixed}(\vec{r})}{\epsilon\epsilon_0} \tag{1.26}$$

where $\vec{r}$ is a general position vector with azimuthal-angle dependence, is performed elsewhere [11]. Here we present it for multi-strand helices taking special care with the numerical factors. We then derive the osmotic pressure of helical interactions in terms of data-fitting parameters. In reciprocal space, Eq. 1.26 becomes

$$\tilde{\Phi}(\vec{q}) = \frac{\tilde{\rho}_{fixed}(\vec{q})}{\epsilon\epsilon_0(q^2 + \kappa^2)} \ , \tag{1.27}$$

where $\tilde{\Phi}(\vec{q})$ and $\tilde{\rho}_{fixed}(\vec{q})$ are Fourier transforms of the potential $\Phi(\vec{r})$ and fixed charge density $\rho_{fixed}(\vec{r})$, respectively, and

$$\{r, \phi, z\} \xrightarrow{\text{F.T.}} \{q_r, q_\phi, q_z\} \ .$$

A continuous infinitely long single-strand helix, aligned parallel to the z-axis with linear charge density λ and radius a, is represented in reciprocal space via [24]

$$\tilde{\rho}_{strand}(q_r, q_\phi, q_z) = \lambda \sum_{n=0}^{\infty} i^n e^{-inq_\phi} J_n(q_r a) \tag{1.28}$$

where $J_n(x)$ are Bessel functions of the first kind of order n. In the summation, the n^{th} term represents momentum transfer in a plane perpendicular to the q_z-axis. Due to the periodicity in the z-direction, $\tilde{\rho}_{strand}(q_r, q_\phi, q_z)$ is nonzero only if $q_z = n\tilde{p}$ for $n = 0, 1, 2, ...$ Here $\tilde{p} = \big(2\pi/\mathrm{P}\big)$ and P is helical pitch length.

These add for a helical structure formed by N strands (with the same a, P, and λ) sharing a common long axis,

$$\tilde{\rho}_{helix} = \tilde{\rho}_{strand,1} + \tilde{\rho}_{strand,2} + ... = \lambda \sum_{n=0}^{\infty} i^n \left[e^{-in\phi_{s1}} + e^{-in\phi_{s2}} + ...\right] J_n(q_r a)$$

where the angles $\phi_{s1}, \phi_{s2}, ...$ describe the orientation of each strand with respect to an arbitrary azimuthal axis. The term in brackets is a Fourier series expansion in the azimuthal angles representing the azimuthal distribution of charges on the molecular surface. In terms of the total linear charge density ($\lambda_0 = N\lambda$) and *helical moments*,

$$\xi_n = \frac{e^{-in\phi_{s1}} + e^{-in\phi_{s2}} + ...}{N} \ , \tag{1.29}$$

a multi-strand helix can be expressed as

$$\tilde{\rho}_{helix} = \lambda_0 \sum_{n=0}^{\infty} i^n \xi_n J_n(q_r a) \ . \tag{1.30}$$

Due to the periodicity along the q_z-axis, $q_z = n\tilde{p}$,

$$q^2 + \kappa^2 = q_r^2 + \kappa_n^2 \tag{1.31}$$

where

$$\kappa_n = \sqrt{\kappa^2 + n^2\tilde{p}^2} \tag{1.32}$$

is the modified decay constant for the n^{th} helical term. Substituting Eqs. 1.30 and 1.31 into Eq. 1.27 yields

$$\tilde{\Phi}(\vec{q}) = \tilde{\Phi}(q_r, q_\phi, n) = \frac{\tilde{\rho}_{helix}(q_r, q_\phi, n)}{\epsilon\epsilon_0(q^2 + \kappa^2)} = \frac{\lambda_0}{\epsilon\epsilon_0}\sum_{n=0}^{\infty} i^n \xi_n \left(\frac{J_n(q_r a)}{q_r^2 + \kappa_n^2}\right) \tag{1.33}$$

where the term in parenthesis describes the q_r dependence of the potential, separated from the azimuthal (ϕ or q_ϕ) dependence (which is contained in ξ_n via Eq. 1.29). Both the radial and azimuthal parts are expressed in terms of n and are related to the periodicity in q_z-direction (i.e., $q_z = n\tilde{p}$ for $n = 0, 1, 2, ...$).

1.3 Hexatic phase data analysis

To sum up, hexatic phase packing is described here with two kinds of interactions: electrostatic and hydration. The bare interaction osmotic pressure of an array of helical molecules (with Wigner-Seitz cell radius R) can be expressed as $\Pi_{bare}(R) = \Pi_e(R) + \Pi_h(R)$, where

$$\Pi_e(R) = \Pi_{e,0}(R) + \Pi_{e,1}(R) + ...$$

$$\Pi_h(R) = \Pi_{h,0}(R) + \Pi_{h,1}(R) + ...$$

and each term in the summations has a different decay constant ($\kappa_{e,n}$ and $\kappa_{h,n}$, respectively) related to the periodicity in the axial direction. The helical moments

$\xi_{e,n}$ describe the distribution of the charged phosphate groups azimuthally on the DNA surface. The helical moments of the duplex DNA (using Eq. 1.29) are

$$\xi_{e,n} = -\frac{1}{2}\Big(e^{-in\phi_{ds}} + e^{+in\phi_{ds}}\Big) = -cos(n\phi_{ds}) \ , \tag{1.34}$$

where $\phi_{ds}\approx 0.4\pi$ is half the azimuthal-width of the minor groove on the duplex B-DNA surface. In the presence of counterions, an azimuthal dependence of charge neutralization on the molecular surface is expected for multivalent counterions. Possible binding sites for the multivalent *condensing* ions are in the grooves between the strands. We assume no specific binding sites on the DNA surface for monovalent counterions. For duplex DNA when the counterions are uniformly distributed,

$$\xi_{e,n} = \Theta - cos(n\phi_{ds}) \ , \tag{1.35}$$

where Θ is the fraction of bare phosphate charges that are neutralized by counterions. Then, $\xi_{e,0} = \Theta - 1$ and $\xi_{e,1} = \Theta - cos\phi_{ds}$. For G-quadruplexes (made of four equally spaced phosphate strands),

$$\xi_{e,n} = \Theta - \frac{1}{4}\left[1 + (-1)^n + 2cos\left(\frac{n\pi}{2}\right)\right] \tag{1.36}$$

when the neutralizing counterions are smeared on the G-quadruplex surface.

However, there is evidence that counterions reside at the center of four stands [17] in the G-quadruplex DNA. When the counterion localization is only on the molecular surface, the interactions can be summarized as follows:

(i) The cylinder interaction term is reduced (net charge is smaller). For the case of nearly complete charge neutralization, cylinder repulsion is negligible.

(ii) The helical moments ($\xi_{e,n}$) are also modified depending on the counterion adsorption pattern on the surface.

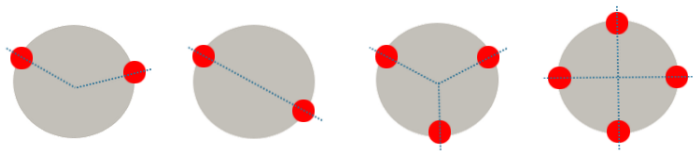

Figure 1.6. Cross-sections of asymmetric duplex (B-DNA), and symmetric duplex, triplex, quadruplex, from left to right, respectively.

	$\lvert\xi_{h,0}\rvert$	$\lvert\xi_{h,1}\rvert$	$\lvert\xi_{h,2}\rvert$	$\lvert\xi_{h,3}\rvert$	$\lvert\xi_{h,4}\rvert$	$\lvert\xi_{h,5}\rvert$
Asymmetric B-DNA duplex (ϕ_{ds}=0.4π)	1	≈0.3	≈0.8	≈0.8	≈0.3	≈0.3
Symmetric duplex (ϕ_{ds}=π)	1	1	1	1	1	1
Symmetric triplex	1	0	0	1	0	0
Symmetric quadruplex	1	0	0	0	1	0

Table 1.1. Helical moments of DNA Structures: The 1st, 2nd, and 3rd-order terms do not contribute to the solution for four-stranded (equally spaced) helices due to symmetry. The apparent decay lengths of the measured osmotic pressure curves in the condensed phases of G-quadruplex DNA (Fig. 2.4) is close to the expected decay length of the 4th order term (≈1Å).

1.3.1 Notes on hydration interactions

In the condensed DNA phases, the molecular motions are strictly confined due to strong interactions with neighboring molecules. In this strict packing one expects the water molecules that are hydrating phosphates to be patterned with the same helicity as the phosphate strands and with the same pattern as the phosphates themselves. Similar to electrostatic interactions, hydration-interaction decay constants are related to the helicity of the DNA chain. The decay length of water structuring is also related to the characteristics of the water molecule [25]. The decay constants of the DNA-DNA hydration-interaction terms are

$$\kappa_{h,n} = \sqrt{\kappa_{h,0}^2 + n^2 \left(\frac{2\pi}{\mathrm{P}}\right)^2} \tag{1.37}$$

where $\kappa_{h,0}$ is the zeroth-order *universal* hydration decay constant, expected to be of order 0.25-0.33Å^{-1}. Short-range hydration interactions (decaying exponentially with

distance from the molecular surface) for close packing of biological molecules is reviewed extensively in the literature [26]. The characteristic decay length is expected to be in the range of 3-4Å, close to the size of the water molecule. When $\kappa_{h,0}$=0.3Å^{-1} (corresponding to a decay length of ≈3.3Å), $\kappa_{h,1}$≈0.34, 0.35Å^{-1}; $\kappa_{h,2}$≈0.43, 0.48Å^{-1}; $\kappa_{h,3}$≈0.55, 0.63Å^{-1}; and $\kappa_{h,4}$≈0.68, 0.80Å^{-1} for B-DNA (P=34Å) and *GMP-quadruplex* DNA (P=40.8Å), respectively.

1.3.2 Summary of the fitting functions and data fittings

The zeroth-order decay constant of the electrostatic interactions $\kappa_{e,0}$ is determined by the solution ionic strength. The expected $\kappa_{h,0}$ (zeroth-order characteristic decay constant of the hydration interactions) is expected to be on the order of ≈0.3Å^{-1}. The decay constants of the higher-order bare-interaction terms (for $n \geq 1$) are modified, depending on the helicity of the DNA molecules (Section 1.2.3).

When DNA samples are equilibrated in PEG solutions, the applied external osmotic pressure Π_{ext} equals the *net repulsion pressure*. In highly condensed packings of DNA helices, $\Pi_{ext}(R) = \Pi_{bare}(R)$. For DNA duplexes, the bare interaction osmotic pressure is dominated by the zeroth-order cylinder terms ($\Pi_{e,0}$ and $\Pi_{h,0}$) and first helical terms ($\Pi_{e,1}$ and $\Pi_{h,1}$):

$$\Pi_{bare}(R) = \Pi_{bare,0}(R) - \Pi_{bare,1}(R). \tag{1.38}$$

The contribution of the second helical terms ($\Pi_{e,2}$ and $\Pi_{h,2}$) to the interaction pressure (at a fixed solution ionic strength) is approximately two orders of magnitude smaller than the contribution of the cylinder terms. The zeroth-order bare interaction pressure is the sum of $\Pi_{h,0}$ and $\Pi_{e,0}$, i.e.,

$$\begin{aligned} \Pi_{bare,0}(R) &= \Pi_{h,0}(R) + \Pi_{e,0}(R) \\ &= \tilde{\Pi}_h \left(\frac{K_0(R/\lambda_{h,0})}{K_1(a/\lambda_{h,0})} \right)^2 + \tilde{\Pi}_e \xi_{e,0}^2 \left(\frac{K_0(R/\lambda_D)}{K_1(a/\lambda_D)} \right)^2 \end{aligned} \tag{1.39}$$

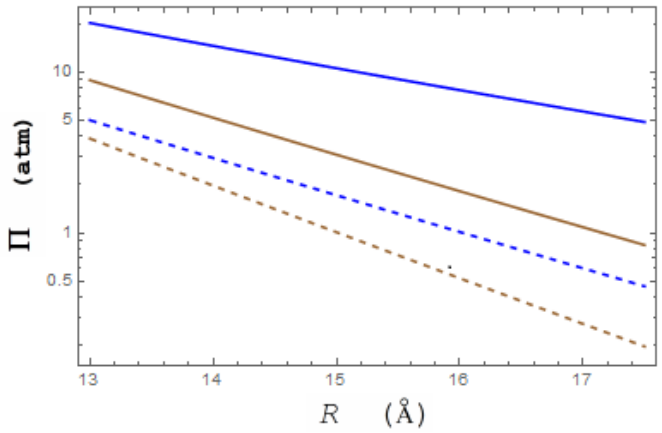

Figure 1.7. Sample calculations: $\Pi_{e,0}$ (solid lines) and $\Pi_{e,1}$ (dashed lines) for duplex B-DNA at [NaCl]=0.1M (blue) and [NaCl]=0.4M (brown). Monovalent Na^+ are assumed to be randomly distributed on the DNA surface and Θ=0.7, i.e., $\xi_{e,0} = -0.3$ and $\xi_{e,1} = 0.7 - cos(0.4\phi_{ds})$ using Eq. 1.35 for duplex B-DNA.

where λ_D is the Debye length $\left(\text{i.e., } \lambda_D{=}\kappa_{e,0}^{-1}\right)$ and $\lambda_{h,0}{=}\kappa_{h,0}^{-1}$. Here $\tilde{\Pi}_e$ (the parameter related to the *bare* surface charge density) is not a fitting parameter: $\tilde{\Pi}_e{\approx}310$ atm for duplex DNA. The parameter $\xi_{e,0}$ is related to charge neutralization where $0 \leq \xi_{e,0} \leq 1$. $\tilde{\Pi}_h$ is determined from the data fittings. In Fig. 1.7 we show sample calculations of $\Pi_{e,0}$ and $\Pi_{e,1}$ for duplex DNA at the lowest and highest NaCl concentrations used in this study, i.e., [NaCl]=0.1M and [NaCl]=0.4M. $\Pi_{e,1}$ are approximately an order of magnitude smaller than $\Pi_{e,0}$ at the [NaCl] concentrations used in our experiments, i.e., 0.1M $\leq$ [NaCl] $\leq$ 0.4M. In the preliminary fits we ignore the term $\Pi_{bare,1}$ in the condensed-phase osmotic-pressure curve-fitting function

$$\Pi_{bare,fit}(R) \approx \Pi_{bare,0}(R) = A_h \left(\frac{K_0(R/\lambda_h)}{K_1(a/\lambda_h)} \right)^2 + \tilde{\Pi}_e \xi_{e,0}^2 \left(\frac{K_0(R/\lambda_e)}{K_1(a/\lambda_e)} \right)^2 . \qquad (1.40)$$

In order to account for this approximation (i.e., ignoring $\Pi_{bare,1}$ which has a contribution of about 10% to Π_{bare}) we replaced the parameters $\tilde{\Pi}_h$, $\lambda_{h,0}$, and λ_D (in the term $\Pi_{bare,0}$) with A_h, λ_h, and λ_e respectively (in the last step of Eqs. 1.39 to 1.40).

[NaCl] in Pairwise Data Sets	A_h (atm)	λ_h (Å)	$\xi_{e,0}^2$
0.1M & 0.2M	992 ± 87	2.25 ± 0.09	0.45-0.50
0.1M & 0.3M	1027 ± 59	2.21 ± 0.06	0.44-0.49
0.1M & 0.4M	955 ± 83	2.29 ± 0.10	0.43-0.50
0.2M & 0.3M	1032 ± 109	2.17 ± 0.12	0.48-0.54
0.2M & 0.4M	971 ± 135	2.23 ± 0.17	0.44-0.56
0.3M & 0.4M	1041 ± 140	2.14 ± 0.16	0.48-0.59

Table 1.2. Results of the simultaneous fits of different combinations of two out of four duplex DNA hexatic phase data sets (i.e., [NaCl]=0.1, 0.2, 0.3, 0.4M) to $\Pi_{bare,fit}$ (Eq. 1.40). See Fig. 1.9 for the fits.

Due to the simplifying assumptions in the fitting functions, the value of $\xi_{e,0}$ extracted from the preliminary fittings (shown below) should not be seen as an exact measure of charge neutralization. The above form $\Pi_{bare,fit}(R)$ is a semi-empirical fitting function rather than a comprehensive description of the interactions.

We use a two-fold fitting strategy. In the first step of our two-fold fitting procedure we simultaneously fit different combinations of two out of four data sets to $\Pi_{bare,fit}$ given in Eq. 1.40. The hydration repulsion parameters (A_h and λ_h) are taken as common and constrained to be the same for all NaCl concentrations, since the osmotic pressure curves for all [NaCl] converge to one curve at small separations. On the other hand, $\xi_{e,0}$ is allowed to vary for different [NaCl]. Although the net molecular charge varies with interaxial separation, we ignore the dependence of $\xi_{e,0}$ on the cell radius in the fits. This is still a reasonable approximation because the charge neutralization occurring in the condensed phase is small (Chapter 3). Finally, for each [NaCl] the decay length of the electrostatic part of the interaction pressure λ_e was allowed to vary within $\pm 10\%$ from the value calculated for the Debye length. We found $\lambda_h \approx 2.2$Å to be approximately the same in all the fits, with an uncertainty of about $\pm 10\%$.

In the second step, we perform a global fitting with four data sets. We fixed λ_h at 2.2Å (extracted in the first step), while A_h and $\xi_{e,0}$ were free parameters. A_h was linked for all [NaCl], and $\xi_{e,0}$ was allowed to vary for different [NaCl]. In this way we

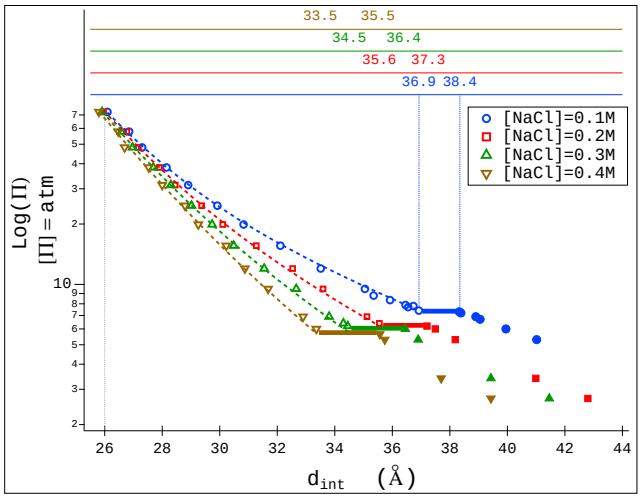

Figure 1.8. Osmotic pressure data for different [NaCl], shown for $d_{int} \geq 26$Å. Less-ordered cholesteric phase data are shown with filled symbols while unfilled symbols represent the hexatic phase data. At low pressures, DNA bundles are in the cholesteric phase. Hexatic−cholesteric transitions take place at transition pressures Π_{tr}≈7.4, 6.3, 6.0, 5.8 atm for [NaCl]=0.1 (blue), 0.2 (red), 0.3 (green), 0.4M (brown), respectively, with abrupt changes in d_{int} (from $d^*_{int,C}$ to $d^*_{int,H}$) at the transition. Π_{tr} , $d^*_{int,C}$ and $d^*_{int,H}$ do not vary significantly for [NaCl] $\geq$ 0.4M. The interaxial separations $d^*_{int,C}$ and $d^*_{int,H}$ are shown in the top axes for [NaCl]=0.1, 0.2, 0.3, 0.4M from bottom to top, respectively. Horizontal lines show the transitions. In the hexatic phase, the overall error in the determination of d_{int} with x-ray diffraction is about 0.1Å. The overall error in the cholesteric phase is bigger (as large as ≈0.2Å) due to the positional disorder and broadening of the diffraction peaks. Upon increasing osmotic pressure in the hexatic phase, d_{int} decreases monotonically, and the osmotic pressure curves for all [NaCl] converge. Here data are shown up to pressure Π≈70 atm, where the differences between the measured d_{int} for the given ionic conditions are ≈0.1Å, i.e., close to the uncertainty of d_{int}. Therefore, in the fits of hexatic phase data to $\Pi_{bare,fit}$ (Eq. 1.40), data from d_{int}=$d^*_{int,H}$ to d_{int}≈26Å are used.

found A_h=1020 atm. The fitting yields the value of the parameter $\xi_{e,0}$≈0.5, about the same for all [NaCl] with an uncertainty ±10%. The results of the simultaneous fits of the duplex DNA hexatic phase data to $\Pi_{bare,fit}$ are shown in Figs. 1.8 and 1.9. For these fittings we used the *IgorPro Global Fitting Package*.

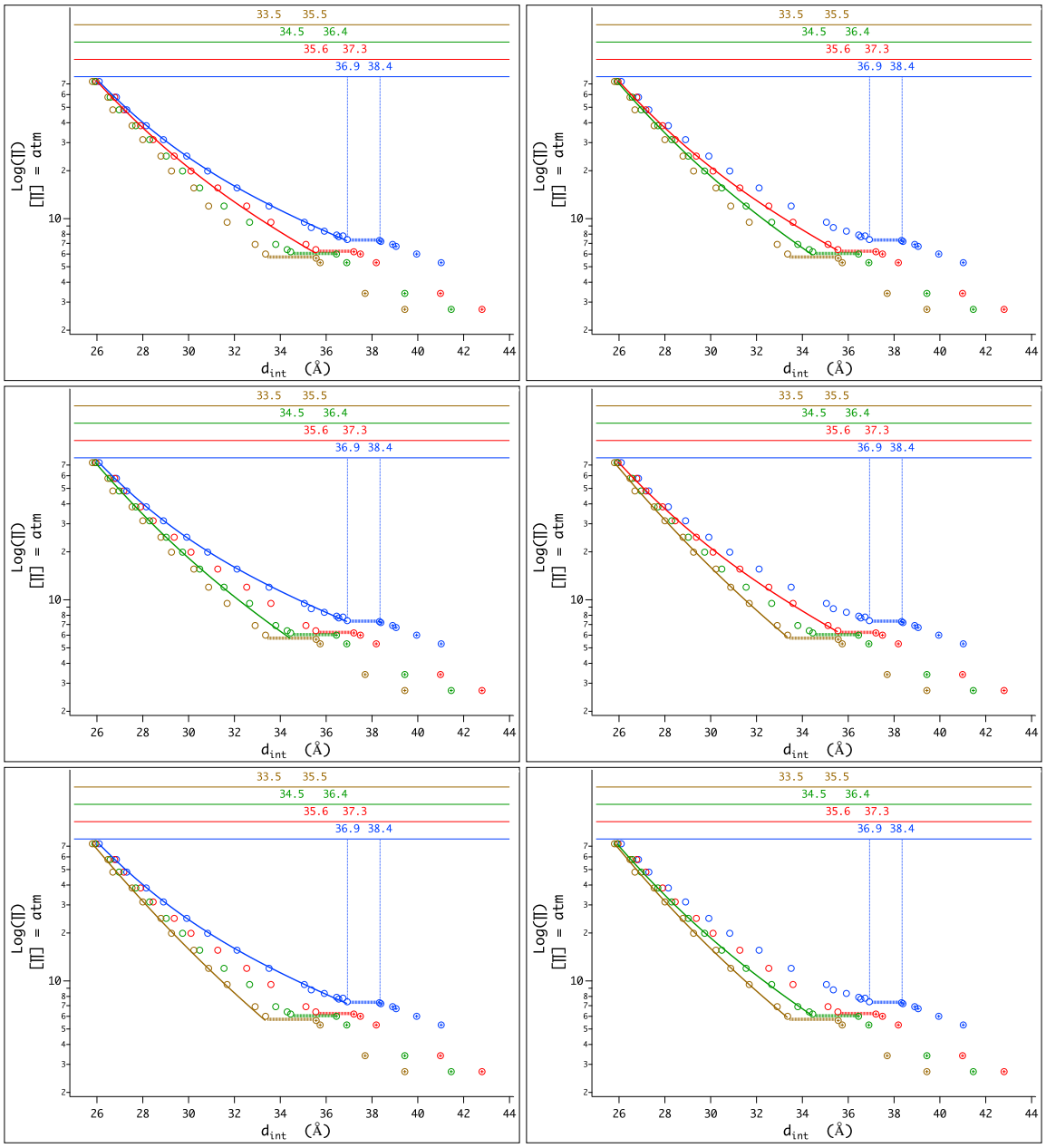

Figure 1.9. Colors and [NaCl] are the same as in Fig. 1.8. Six different combinations of two out of four data sets are fitted simultaneously to $\Pi_{bare,fit}$ (Eq. 1.40) in order to extract the common hydration repulsion decay length λ_h for duplexes. In these fits, the hydration parameters (A_h and λ_h) were linked for all [NaCl]. In order to allow for the fact that we ignored the *helicity-dependent* part of the osmotic pressure (i.e., $\Pi_{bare,1}$) in the fits, λ_e were allowed to vary within $\pm 10\%$ from their calculated values (using λ_D=3.05Å/$\sqrt{I(M)}$, i.e., λ_D≈9.7Å, 6.9Å, 5.6Å, 4.9Å for [NaCl]=0.1, 0.2, 0.3, and 0.4M, respectively. $\xi_{e,0}$ was allowed to vary for different [NaCl]. The results of these fits are given in Table 1.2.

1.4 Positional disorder and the cholesteric phase

One can define the free energy (per DNA molecule) in the fluctuating cholesteric phase as the sum of the bare interaction free energy (F_{bare}) and the fluctuational free energy (F_{fl}), i.e.,

$$F_{chol} = F_{bare} + F_{fl} \ .$$

Here F_{fl} describes the free energy due to positional disorder (i.e., chain density fluctuations) relative to the condensed phase (i.e., the hexatic phase for duplex DNA) where fluctuation effects are negligible. V_{cell} is the volume of a cell containing a single DNA chain in the cylindrical cell model, i.e., $V_{cell} = \left(\pi R^2\right) L$, where R is the radius of the cylindrical Wigner-Seitz cell and L is the length of a single DNA chain. In the cylindrical cell model, the thermodynamic relation for the osmotic pressure ($\Pi = -\partial F/\partial V$) reduces to

$$\Pi = -\frac{\partial F}{\partial V} = -\frac{\partial F_{chol}}{\partial V_{cell}} = -\frac{1}{2\pi RL}\frac{\partial F_{chol}}{\partial R} \ . \tag{1.41}$$

1.4.1 Gaussian fluctuations

The radial intensity profiles $I(q)$ vs. q are obtained by radial integration of the intensity distributions in 2D raw x-ray images. First-order diffraction peaks in the disordered phase are fitted to

$$G_q(q, q_0, \sigma_q) = \frac{1}{\sqrt{2\pi\sigma_q^2}} e^{-\left[\frac{(q-q_0)^2}{2\sigma_q^2}\right]} \tag{1.42}$$

i.e., a Gaussian centered at q=q_0 with standard deviation σ_q. This Gaussian describes the probability distribution of the measured momentum transfer q. The mean-square fluctuation of q is $\langle q^2 \rangle = \sigma_q^2$. The corresponding standard deviation of the Wigner-Seitz cell radius can also be calculated from this Gaussian distribution.

We explored the dependence of positional disorder on two independent thermodynamic variables, external osmotic pressure Π_{ext} and ionic strength. Diffraction peaks

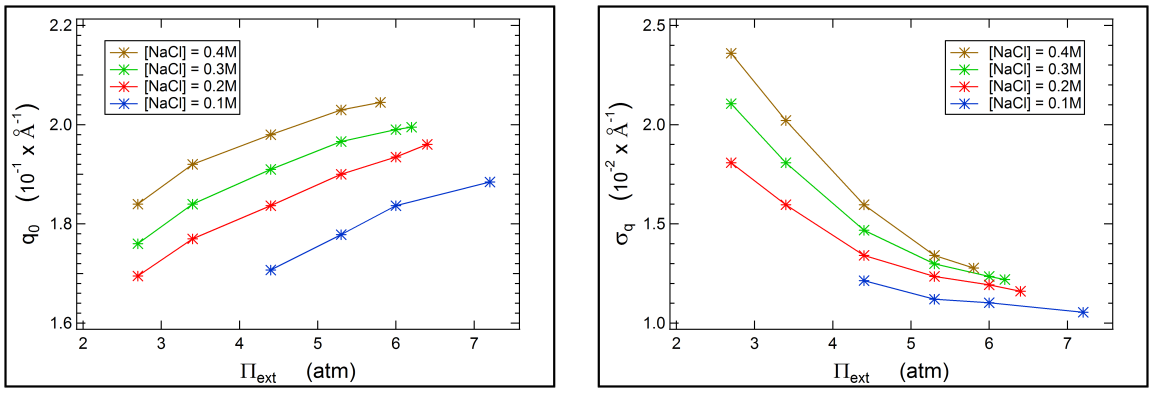

Figure 1.10. The dependence of the center of the Gaussian diffraction peak q_0 (left) and its standard deviation σ_q (right) on the external osmotic-pressure. The error in the determination of σ_q is $\approx 0.001 \text{Å}^{-1}$. The procedure for the x-ray diffraction peak fittings is described in Chapter 5.

can be fitted to Gaussian shapes (Eq. 1.42). Details of the fitting are explained in Chapter 5. Fig. 1.10 shows the measured q_0 and σ_q under different applied osmotic pressures for [NaCl]=0.1M, 0.2M, 0.3M, and 0.4M.

1.4.2 Fluctuational free energy

For fitting purposes, we use an empirical fluctuational free energy, derived in Ref. [27], due to the radial-chain density fluctuations in a hexagonal array of chain molecules:

$$F_{fl} \approx \mathrm{k_B T} (q_{max})^{5/2} \left[\frac{V_{cell}}{5\ 2^{3/2}\pi} \left(\frac{B_b}{K} \right)^{1/4} \right] , \tag{1.43}$$

where B_b and K are the bare bulk modulus and bending elastic constant of the DNA cholesteric phase, respectively. K is defined as

$$K = \rho K_c = \frac{K_c}{\pi R^2} ,$$

where ρ is the 2D number density of DNA chains in the plane perpendicular to their helical axes. K_c=$(k_B \mathrm{T}) L_p$ is the bending rigidity of a single DNA chain, where L_p is

the persistence length. The effect of [NaCl] on the persistence length of duplex DNA (L_p≈500Å) is less than 5% for 0.1M ≤ [NaCl] ≤ 0.4M [28].

We replace q_{max} with a scaling prefactor (c) times the Brillouin-zone (per DNA chain) radius,

$$q_{max} \rightarrow c\left(\frac{\pi}{2R}\right).$$

Substituting V_{cell}, K, and q_{max} in Eq. 1.43 yields free energy per unit length,

$$\frac{F_{fl}(R)}{L} = k_B\mathrm{T}\left[\frac{c^{5/2}\pi^{11/4}}{80}\left(\frac{B_b}{K_c}\right)^{1/4}\right], \tag{1.44}$$

where L is the length of the DNA chains. Thus, using K_c=$(k_B\mathrm{T})L_p \approx 2\times10^3$ atm(nm)^4 for duplex DNA,

$$\frac{F_{fl}(R)}{L} \approx 0.044c^{5/2}B_b^{1/4}\frac{k_B\mathrm{T}}{\mathrm{nm}}\ , \tag{1.45}$$

when B_b is in units of atm.

1.4.3 Analysis of the cholesteric phase data

The osmotic pressure due to bare interactions is $\Pi_{bare}(R) = \Pi_e(R) + \Pi_h(R)$. The molecules are not azimuthally oriented in the fluctuating phase, and higher-order helical terms ($n \geq 1$) do not contribute to the bare interaction pressure (Section 1.3). For n=0 (cylinder terms),

$$\Pi_e(R) = \Pi_{e,0}(R) \;=\; \tilde{\Pi}_e\left(\frac{K_0(\kappa_{e,0}R)}{K_1(\kappa_{e,0}a)}\right)^2 \tag{1.46}$$

$$\Pi_h(R) = \Pi_{h,0}(R) \;=\; \tilde{\Pi}_h\left(\frac{K_0(\kappa_{h,0}R)}{K_1(\kappa_{h,0}a)}\right)^2 \tag{1.47}$$

where $\tilde{\Pi}_e$ and $\tilde{\Pi}_h$ are constants in units of atm (see Section 1.2.2 for the definitions and Section 1.3 for the measured values of $\tilde{\Pi}_e$ and $\tilde{\Pi}_h$). The decay constant of the short-range hydration repulsion $\kappa_{h,0}$ is significantly larger than the decay constant of the

electrostatic repulsion $\kappa_{e,0}$ (Section 1.3). Near the hexatic−cholesteric transition the relative contribution of hydration repulsion Π_h to the total bare interaction repulsion is 1-2 orders of magnitude smaller than the contribution of the electrostatic term Π_e. For example, when R=20Å, $\Pi_h(R)$ is approximately 1% of $\Pi_e(R)$ for [NaCl]=0.1M and 5% of $\Pi_e(R)$ for [NaCl]=0.4M (Section 1.3).

The 2D bare bulk modulus is defined as the change of the bare interaction pressure per fractional change of the cell area, i.e.,

$$B_b = -A_{cell}\frac{\partial \Pi_{bare}}{\partial A_{cell}} = -(\pi R^2)\frac{\partial \Pi_{bare}}{\partial(\pi R^2)} \ . \tag{1.48}$$

Using Eqs. 1.46-1.47, and

$$\frac{dK_0(x)}{dx} = -K_1(x) \ ,$$

we find

$$\frac{\partial \Pi_{bare}(R)}{\partial R} = -2\left[\kappa_e\tilde{\Pi}_e\frac{K_0(\kappa_e R)K_1(\kappa_e R)}{K_1^2(\kappa_e a)} + \kappa_h\tilde{\Pi}_h\frac{K_0(\kappa_h R)K_1(\kappa_h R)}{K_1^2(\kappa_h a)}\right] .$$

Then, using

$$B_b = -(\pi R^2)\frac{\partial \Pi_{bare}}{\partial(\pi R^2)} = -\frac{1}{2}\left[R\frac{\partial \Pi_{bare}}{\partial R}\right] ,$$

we find

$$B_b = (\kappa_e R)\tilde{\Pi}_e\frac{K_0(\kappa_e R)K_1(\kappa_e R)}{K_1^2(\kappa_e a)} + (\kappa_h R)\tilde{\Pi}_h\frac{K_0(\kappa_h R)K_1(\kappa_h R)}{K_1^2(\kappa_h a)} \ . \tag{1.49}$$

For duplex DNA in the *fluctuating* phase at DNA densities near the transition to the *condensed* phase, the second term in Eq. 1.49 is approximately one order of magnitude smaller than the first term. The fluctuation part of the osmotic pressure scales with the relative change in the logarithm of the bare bulk modulus with changing cell area (see below). Therefore, the overall effect of ignoring the second term in

Eq. 1.49 on the fits and on the calculations of the fluctuation osmotic pressure Π_{fl} is negligible. The variation of B_b with R for different [NaCl] is shown in Fig. 1.11-a. Additionally, the variation of F_{fl}/L with R for different [NaCl] when c=1 is shown in Fig. 1.11-b. There are 6 nucleotides per nanometer length of duplex DNA. The calculated F_{fl}/L (in units of k_BT per nanometer) correspond to ≈1-1.5% of k_BT per nucleotide (when c=1) near the condensation transition.

It is convenient to write the fluctuational free energy (Eq. 1.44) as

$$\frac{F_{fl}(R)}{L} = \alpha B_b^{1/4}$$

with

$$\alpha = k_B\mathrm{T}\left(\frac{\pi^{11/4}\ c^{5/2}}{80\ K_c^{1/4}}\right).$$

Using

$$\frac{\partial(F_{fl}(R)/L)}{\partial R} = \alpha\frac{B_b^{-3/4}}{4}\frac{\partial B_b}{\partial R} = \frac{1}{4}\Big[\alpha B_b^{1/4}\Big]\frac{\partial \log B_b}{\partial R} = \frac{1}{4}\left[\frac{F_{fl}(R)}{L}\right]\frac{\partial \log B_b}{\partial R}\ ,$$

with Eqs. 1.41 and 1.45, we find

$$\Pi_{fl}(R) = -\frac{1}{2\pi R}\frac{\partial(F_{fl}(R)/L)}{\partial R} = \Pi_{fl}^{*}\left(-(\pi R^2)\frac{\partial \log B_b}{\partial(\pi R^2)}\right). \tag{1.50}$$

For duplex DNA

$$\Pi_{fl}^{*}(R) = \frac{F_{fl}(R)/L}{4\pi R^2} \approx 13.8\frac{c^{5/2}B_b^{1/4}}{R^2}\ \text{atm}\ , \tag{1.51}$$

with R in units of Å and B_b in units of atm. The variation of Π_{fl}^{*} with R for different [NaCl] when c=1 is shown in Fig. 1.11-c. In order to calculate Π_{fl} vs. R, we use quadratic fits to $\log B_b$ vs. R data (Fig. 1.11-d). The calculated Π_{fl} as a function of R, when c=1, is also shown in Fig. 1.11-e.

The scaling prefactor c in F_{fl} is related to DNA-chain motions in the fluctuating phase. One can obtain information about the chain-fluctuation modes (and thus

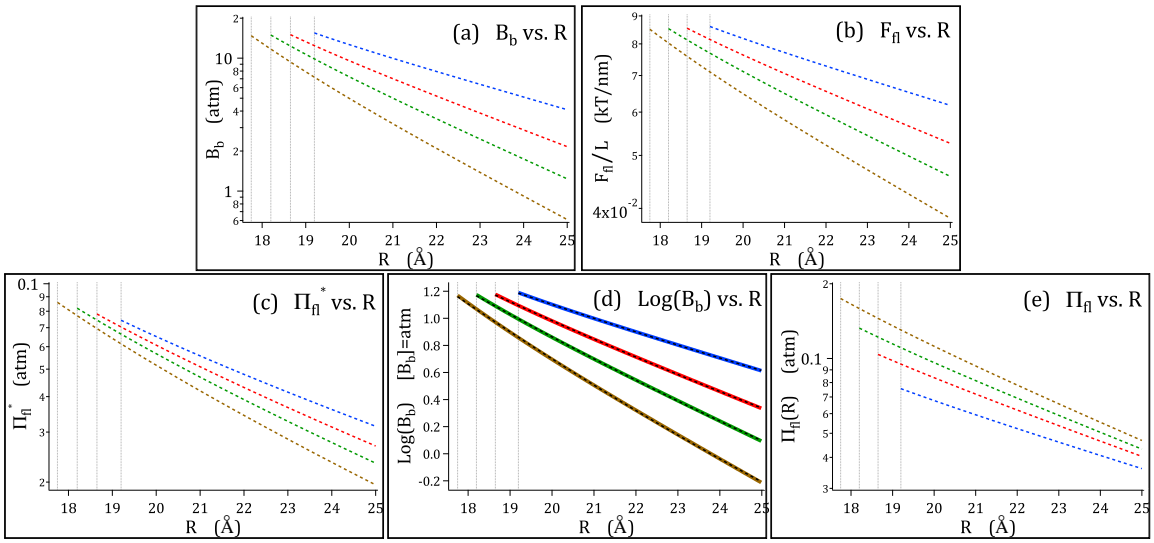

Figure 1.11. Colors and [NaCl] are the same as in Fig. 1.8. Thin vertical lines show the smallest cell radii in the cholesteric phase, i.e., R=R_C^*, for [NaCl]=0.1, 0.2, 0.3, 0.4M, from right to left, respectively. (a): B_b vs. R. (b): F_{fl}/L vs. R when c=1. (c): Π_{fl}^* vs. R when c=1. (d): Thick colored lines show the variation of $\log B_b$ with R. We calculate the logarithmic derivative of B_b (Eq. 1.50) using quadratic fits (thin dashed lines). (e): Calculated Π_{fl} vs. R when c=1.

about the fluctuational free-energy scaling) from the x-ray diffraction peak widths (Fig. 1.10). We have shown in this section that one can calculate the bare bulk modulus (B_b) from the measured external osmotic pressure dependence of the cell radius in the condensed phase. The differences between fluctuation osmotic pressures for different [NaCl] decrease with increasing R when c=1 (Fig. 1.11), i.e, when the dependence of c on the external osmotic pressure and ionic strength is ignored.

The B_b in the fluctuating phase can be found more accurately by noting the change of bare interaction pressure occurring at the transition (Chapter 3). In the calculations performed in this section, we have not taken into account the interaxial dependence of the charge neutralization and its effect on the bare electrostatic interaction. Additionally, for a more accurate analysis, one must account for the dependence of the fluctuation modes that contribute to the fluctuational free energy. This information can be obtained from x-ray diffraction peak-widths (Fig. 1.10).

CHAPTER 2

X-RAY CHARACTERIZATION OF MESOPHASES OF HUMAN TELOMERIC G-QUADRUPLEXES AND OTHER DNA ANALOGUES

2.1 Motivation

Human telomeric sequences $AG_3\left(TTAG_3\right)_n$ can form four-strand G-quadruplexes [29] by folding on themselves and matching the G_3 segments, enabling the formation of G-quartets [3,4]. In particular, G-quadruplex conformations of the four-repeat human telomere $AG_3\left(TTAG_3\right)_3$ in the presence of K^+ ions have been an important research focus [29, 30]: The parallel-stranded conformation is observed in the crystalline state [31] and in K^+ solutions [32, 33] in the presence of PEG. G-quadruplexes formed by the four-repeat human telomere have been shown [34] to be thermally more stable than the structures formed by the longer telomeric sequences, implying that the four-repeat telomere is the likely candidate for G-quadruplex formation in human cells [35]. Additionally, molecular crowding conditions are known to critically affect the structure of G-quadruplexes *in vivo* [36]. We systematically varied the osmotic pressure exerted by the bathing PEG solutions and examined the liquid-crystalline phase behavior of the *22-mer HT-quadruplex* in order to assess its likely state under similar crowded conditions in the cellular environment.

2.2 Background and Introduction

The parallel-stranded intramolecular G-quadruplex formed by $AG_3\left(TTAG_3\right)_3$ will be referred to as the *22-mer HT-quadruplex*. This G-quadruplex [31] (PDB: 1KF1)

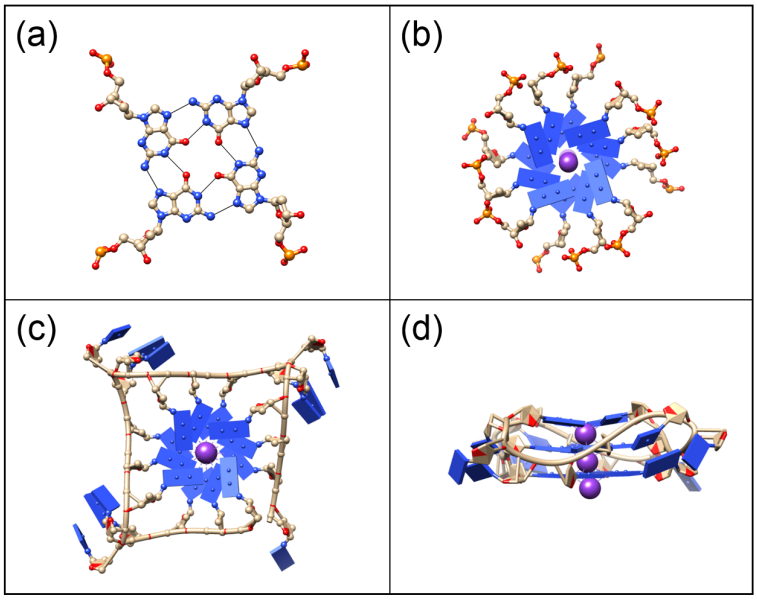

Figure 2.1. Schematic representations of the structures: (a) G-quartet made of four GMP monomers. Thin black lines represent the hydrogen bonds holding nucleotides together in a planar cyclic arrangement. (b) Top view of the *GMP-quadruplex* in ordered columnar phase, where stacking is helical with an azimuthal rotation of 30 ° between adjacent G-quartets [17]. (c) Top view of the parallel-stranded *22-mer HT-quadruplex* (PDB: 1KF1) formed by the sequence $AG_3(TTAG_3)_3$. In this conformation (observed in the crystalline state [31] as well as in the non-crystalline state under molecular crowding conditions [32,33]), four parallel GGG runs form a stack of three planar G-quartets in the central core and TTA segments fold into loops projecting outwards. (d) Side view of the *22-mer HT-quadruplex*. K^+ ions (purple) reside inside the G-quadruplexes and they are positioned between the adjacent G-quartets. G-quartets in a & b are modeled from *22-mer HT-quadruplex*.

contains a central core formed by the stacking of three G-quartets supported by four parallel sugar-phosphate strands and TTA linkers that connect the adjacent strands by forming side-loops (Fig. 2.1-c & 2.1-d).

The G-quartet is a planar structure formed by the cyclic arrangement of four hydrogen-bonded guanine residues. We first examined the liquid-crystalline phases of the G-quartets that are made of four GMP monomers [17] (Fig. 2.1-a). The columnar structure built by the stacking of such G-quartets (abbreviated *GMP-quadruplex*) is a simple model of biologically relevant G-quadruplexes. Helical stacking of G-

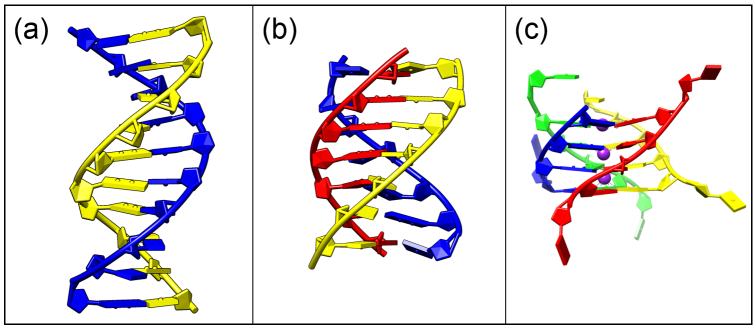

Figure 2.2. Schematic representations of the other DNA structures considered in this manuscript: (a) Side view of the duplex DNA in its B-form. (b) Side view of the triplex DNA (PDB: 134D). We used *Poly(AT*T)-triplex* made of 50 bases long Poly(A) and Poly(T) oligonucleotides [45] in the presence of Mg^{2+} (explained in the text). (c) Side view of the intermolecular parallel-stranded TG_4T*-quadruplex* (PDB: 244D) made of four TG_4T oligonucleotides. In this quadruplex [42], G-quartets are formed by hydrogen-bonding of the four parallel GGGG runs. Unlike the *GMP-quadruplex*, in the TG_4T*-quadruplex*, G-quartets are connected via four sugar-phosphate strands. Similar to the other quadruplex structures (shown in Fig. 2.1), K^+ ions (purple) reside inside the TG_4T*-quadruplex*. In this figure, we used non-standard color-coding for the bases in order to differentiate between different strands of the structures.

quartets (Fig. 2.1-b) in the crystalline state was proposed based on fiber diffraction [17]. Formation of columnar structures was detected also in the non-crystalline GMP solutions in the presence of K^+ ions [37]. By varying the osmotic pressure of the solution set by the concentration of PEG, we investigated the first-order transition from a loosely linked and disordered G-quartet column formed in K^+ solution to the highly-ordered *GMP-quadruplex* driven by the osmotic pressure changes in the regime mimicking the biologically relevant molecular crowding conditions. This osmotic-pressure-induced change in order along the columnar axis consequently permits tighter packing of the *GMP-quadruplex* array between the columns, with progressively longer-ranged hexagonal order in the plane perpendicular to the columnar axis.

The columnar liquid-crystalline mesophases of planar disc-shaped structures are known and understood [38]. In these phases, disc-shaped structures are stacked on

top of each other and form columns, which in turn self-assemble into arrays. As with other columnar assemblies [20], the nature of intra- and intercolumnar ordering can vary, depending on solution conditions. The disordered columnar phases (Φ_{dc}) exhibit fluid-like positional intracolumnar order, while in the ordered columnar phases (Φ_{oc}) there is long-range positional order within each column. This leads to column-column positional and orientational correlations and consequently to long-range intercolumnar order [20, 39]. In this respect, the mesophase transition of *GMP-quadruplex* is similar to the $\Phi_{dc} \rightarrow \Phi_{oc}$ transitions observed in the columnar aggregates of other disc-shaped structures built from the molecules with aromatic rings [38–40].

Recent experiments demonstrated that the formation of higher-order G-quadruplex motifs in the human telomere is sensitive to the phase in the cell-cycle [35], which is related to molecular crowding that can tune gene expression [41]. Thus, the $\Phi_{dc} \rightarrow \Phi_{oc}$ transition of the *GMP-quadruplex* induced by changing molecular-crowding conditions is relevant for the higher-order G-quadruplex structure formation built from the *22-mer HT-quadruplex* repeats [31, 34]. We examined the columnar assemblies and the mesophase behaviors of (i) the *22-mer HT-quadruplex* and (ii) the intermolecular parallel-stranded G-quadruplex formed by four TG_4T oligonucleotides [42] (PDB:244D). The latter (abbreviated *TG_4T-quadruplex*) is shown in Fig. 2.2-c. This quadruplex was selected because of its resemblance to the *22-mer HT-quadruplex*. In both structures, parallel sugar-phosphate backbones interconnect the stacked G-quartets. Contrary to the *22-mer HT-quadruplex*, the *TG_4T-quadruplex* is also missing the flexible side loops.

The $\Phi_{dc} \rightarrow \Phi_{oc}$ transition of the *GMP-quadruplex* is also analogous to the mesophase transitions in duplex and triplex DNA arrays under similar crowding conditions. We described this transition for duplexes (cholesteric-hexatic transition) in Chapter 1. While the columnar hexagonal phase of the DNA triplexes has been observed before [43], the triplex mesophase transition was not measured. The changes observed

in the x-ray diffraction patterns at the mesophase transitions of the duplex, triplex, and G-quadruplex are essentially similar.

Finally, *22-mer HT-quadruplex* has a propeller-like shape [31] though not as pronounced as when *22-mer HT-quadruplex* blocks are stacked in a column with TTA *linkers* between them [29, 31]. In this particular model for the columnar stacking of G-quadruplex blocks (that are formed by four-repeat telomeric sequences), TTA segments connect the consecutive blocks that in turn would form an ordered G-quadruplex column with quasi-continuous helical characteristics.

The subject of focus in this chapter is the columnar mesophase behavior of *unlinked 22-mer HT-quadruplex* blocks. These are similar to the unlinked very-short duplex DNA fragments [44], except that the strong stacking interactions between the exposed hydrophobic cores of the duplex DNA fragments [44] are missing in the *22-mer HT-quadruplex* case.

2.3 Results

Under sufficient molecular crowding (see Chapter 5), duplex and quadruplex (*GMP-quadruplex*, *22-mer HT-quadruplex*, and *TG_4T-quadruplex*) DNA structures self-assemble into stable aggregates in the presence of K^+ ions without any other ions being added. These aggregates were transferred into PEG solutions of various concentrations for equilibration against known *external* osmotic pressures. PEG is excluded from the DNA arrays during equilibration. Temperature-dependent osmotic pressures produced by the solutions of PEG at various concentrations are from [7]. Unless otherwise stated, all the measurements are at [KCl]=0.3 M.

Increasing order continuously with increasing osmotic compression in the disordered columnar mesophase (Φ_{dc}) is followed by a sudden collapse into the ordered columnar mesophase (Φ_{oc}), with remarkable changes in the intercolumnar distance (d_{int}) and the radial order (Fig. 2.3). At the $\Phi_{dc} \rightarrow \Phi_{oc}$ transition of the *GMP-*

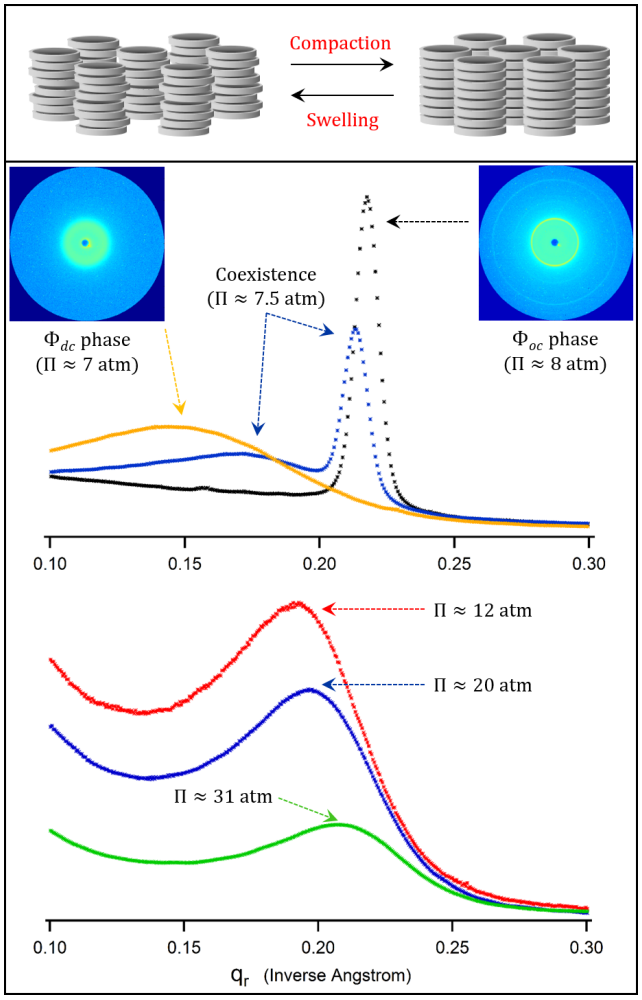

Figure 2.3. Upper panel: Schematic illustration of the hexagonal columnar liquid-crystalline phases of G-quartets. In the Φ_{dc} phase (left), G-quartets in each column are displaced laterally around average columnar axes. In the Φ_{oc} phase (right), both G-quartet correlations within each column and column-column correlations are long-range. At the $\Phi_{dc} \rightarrow \Phi_{oc}$ transition, intercolumnar spacings between the neighboring columns (d_{int}) decrease by 6.5-7Å. **Middle panel:** 1D intensity profiles (i.e., x-ray scattering intensities vs. momentum transfer in the radial direction) from *GMP-quadruplex* arrays at [KCl]=0.3 M, showing the $\Phi_{dc} \rightarrow \Phi_{oc}$ transition. Essentially similar patterns were obtained with the duplex (Fig. 2.2-a), triplex (Fig. 2.2-b), and intermolecular TG_4T*-quadruplex* (Fig. 2.2-c). In the course of the $\Phi_{dc} \rightarrow \Phi_{oc}$ transition, the shape of the diffraction peak changes dramatically while the peak center is shifted to a higher q_r value. Two distinct types of peaks in the intensity profile coexist over a small range of Π , i.e., a phase-coexistence region. The procedure for x-ray diffraction peak fits is described in Chapter 5. **Insets:** X-ray images of the *GMP-quadruplex* arrays in the Φ_{dc} (left) and Φ_{oc} (right) phases. Higher-order diffraction rings in the x-ray images of the Φ_{oc} phase confirm hexagonal packing. **Lower panel:** 1D intensity profiles from *22-mer HT-quadruplex* (Fig. 2.1-c & Fig. 2.1-d) arrays at [KCl]=0.3 M.

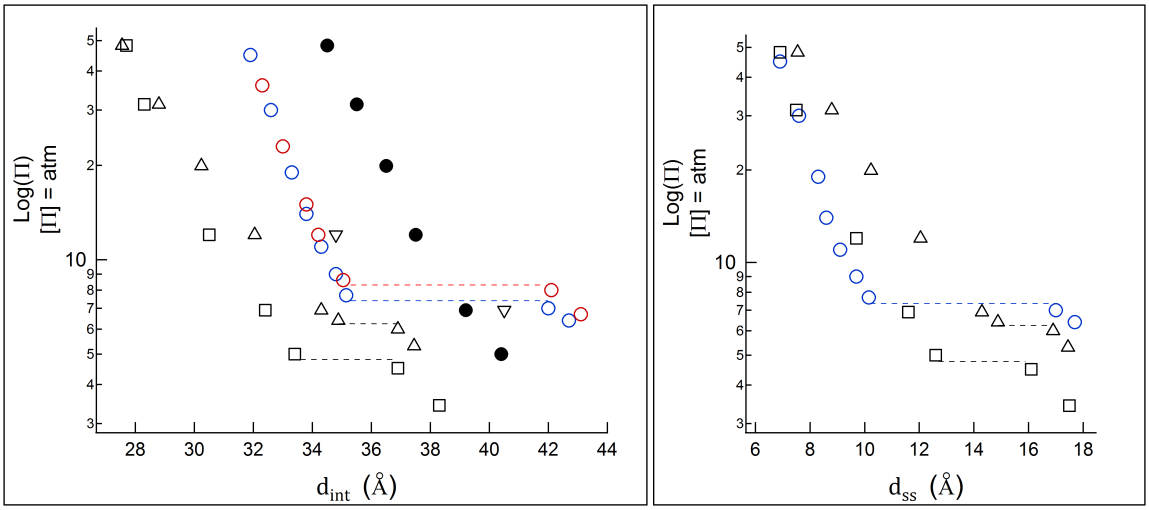

Figure 2.4. Left: Osmotic pressure vs. intercolumnar (interaxial) spacings (d_{int}) for all structures that are shown in Fig. 2.1 & Fig. 2.2: Duplex (triangle), *Poly(AT*T)-triplex* (square), *GMP-quadruplex* (circle), *22-mer HT-quadruplex* (filled circle), *TG_4T-quadruplex* (inverted triangle). Horizontal lines show the $\Phi_{dc} \rightarrow \Phi_{oc}$ transitions. The lines are drawn approximately between the two d_{int} values determined from the centers of the coexisting two peaks in the phase-coexistence region (see Fig. 2.3). *Poly(AT*T)-triplex* measurements are performed under [MgCl]=5 mM and [KCl]=0.3 M. The measurements with other DNA structures are at [KCl]=0.3 M in the absence of any other ions. The effect of temperature is shown only for *GMP-quadruplex* (where blue and red symbols show the measurements at 20 and 40 °C, respectively, when the osmotic pressures are corrected for temperature). The slight temperature dependence of the transition pressure is discussed in the text. **Right:** Osmotic pressure vs. surface-to-surface separation (d_{ss}) for duplex, *Poly(AT*T)-triplex*, and *GMP-quadruplex* DNA. Here, $d_{ss} = d_{int} - 2a$, where a is the molecular (or columnar) radius ≈10Å, 10.4Å, 12.5Å for duplex [16], *Poly(AT*T)-triplex* [46], and *GMP-quadruplex* [17], respectively.

quadruplex, in particular, the change in the intercolumnar distance (Δd_{int}) is about 6.5-7 Å (Fig. 2.4). This change in the packing density corresponds to about 0.3-0.4 nm^3 volume change per GMP nucleotide. It occurs concurrently with a significant lowering of packing disorder. The radial disorder in the Φ_{dc} phase, due to lateral displacements of loosely stacked G-quartets around the mean columnar axis, is evident in the Gaussian-shaped broad diffraction radial intensity peaks. By comparison, the Lorentzian peak shape in the Φ_{oc} phase attests to the long-range nature of positional

order. The correlation length in the ordered phase (equal to the inverse of the full-width-at-half-maximum of a Lorentzian function fitted to the x-ray diffraction radial intensity peak) is 5-to-6 neighbor separations for duplex DNA and 9-to-10 neighbor separations for *GMP-quadruplex*.

The slight temperature sensitivity of the $\Phi_{dc} \rightarrow \Phi_{oc}$ transition is shown for *GMP-quadruplex* (open circles in Fig. 2.4). Temperature has no detectable effect on the packing density in the Φ_{oc} phase. The transition osmotic pressure $\left(\Pi_{tr}\right)$ increases by about 1 atm upon increasing temperature from 20 to 40 °C. The effect of temperature on Π_{tr} is appreciably smaller for other structures and not shown. Phase-coexistence is pronounced over a significantly narrower range of osmotic pressures in the transitions of the duplex and *GMP-quadruplex* than in the transitions of the other structures. In particular, for *GMP-quadruplex*, the width of the phase-coexistence region is about 0.5 atm osmotic pressure.

The osmotic pressures required for inducing DNA-analogue mesophase transitions strongly depend on solution ionic conditions. At $[K^+]$=0.3 M, in the absence of any multivalent salts, the transition osmotic pressures for duplex and *GMP-quadruplex* are about the same (Fig. 2.4), varying nearly from 6 to 8 atm (corresponding to from ≈19 to ≈22 wt% PEG 8000 concentration at 20 °C). Increasing K^+ concentration (under fixed external pressure) results in compression in the arrays of duplexes and G-quadruplexes. This observation can be explained as the screening of the electrostatic interactions between intercolumnar phosphate charges. (See below for triplexes.)

***22-mer HT-quadruplex*:** With the aim of obtaining ordered columnar phases of the *22-mer HT-quadruplex* arrays (similar to the Φ_{oc} phase of simpler model *GMP-quadruplex*), we increased the osmotic pressure compressing the disordered arrays of *22-mer HT-quadruplex* and measured their x-ray diffraction patterns. The radial packing order increases with increasing osmotic compression (Fig. 2.5). However, the very sharp changes observed in the radial intensity profiles at the first-order

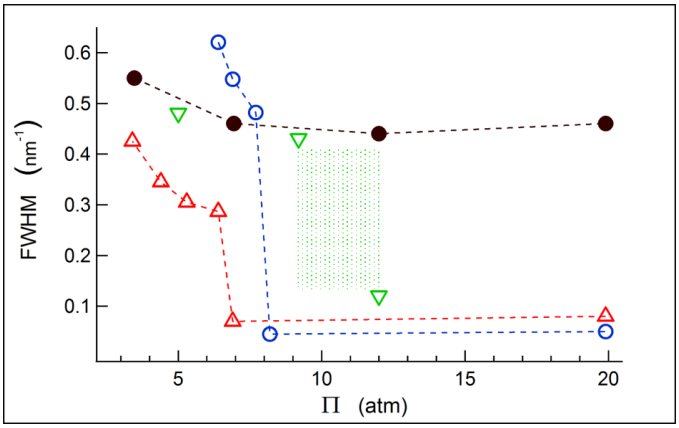

Figure 2.5. FWHM of the x-ray diffraction radial intensity peaks from duplex (red triangle), *GMP-quadruplex* (blue circle), *22-mer HT-quadruplex* (black filled circle), and TG_4T*-quadruplex* (green inverted triangle) arrays. In the less-ordered phases (Φ_{dc}), packing disorder decreases with increasing osmotic pressure for all structures. Further compression leads to $\Phi_{dc} \rightarrow \Phi_{oc}$ transitions with discontinuous changes in the packing order in duplex and *GMP-quadruplex* arrays, which occur concurrently with discontinuous changes in the packing densities (shown in Fig. 2.4). The latter is not observed in the *22-mer HT-quadruplex* arrays (discussed in the text). Phase-coexistence is shown only for the TG_4T*-quadruplex* (green shaded area). Phase-coexistence is observed over significantly narrower ranges of osmotic pressures for the duplex and *GMP-quadruplex* compared with the TG_4T*-quadruplex* (discussed in the text). Finally, the error in the determination of FWHM is as big as $\approx 0.1\text{nm}^{-1}$ in the case of broad Gaussian peaks (in the disordered phases). The errors in FWHM are smaller for the sharp Lorentzian peaks in the ordered phases (see Chapter 5).

$\Phi_{dc} \rightarrow \Phi_{oc}$ transition of the *GMP-quadruplex* are not seen in the radial intensity profiles of *22-mer HT-quadruplex* arrays (Fig. 2.3).

When equilibrated under osmotic pressures less than the $\Phi_{dc} \rightarrow \Phi_{oc}$ transition osmotic pressure of the *GMP-quadruplex*, the measured positional disorder in *22-mer HT-quadruplex* array is smaller than the disorder in *GMP-quadruplex* array at the same pressure (Fig. 2.5), which can be argued to be a consequence of the constrained lateral motion of the G-quartets, connected by the sugar-phosphate backbone. This connectivity increases the stability of *22-mer HT-quadruplex* relative to the *GMP-quadruplex* and decreases its positional as well as stacking disorder. This is obviously true despite the TTA loops of the *22-mer HT-quadruplex* that extend laterally from

the core G-quartets [31], which could be conceived as promoting and not suppressing the disorder of the columns. However, when equilibrated under osmotic pressures greater than that of the $\Phi_{dc} \rightarrow \Phi_{oc}$ transition of *GMP-quadruplex*, d_{int} is 2-3 Å bigger for *22-mer HT-quadruplex* than for *GMP-quadruplex* at the same pressure (Fig. 2.4). Under these conditions, the radial disorder in the *22-mer HT-quadruplex* array remains almost the same as in the disordered phase, while that of the *GMP-quadruplex* array drops significantly (Fig. 2.5, blue circles), possibly signaling the reverse action of laterally extended TTA loops in this case, amounting to a simple increase of the effective diameter of the columns.

***TG_4T-quadruplex*:** When we followed the same procedure with the intermolecular *TG_4T-quadruplex*, we observed first-order transitions similar to the $\Phi_{dc} \rightarrow \Phi_{oc}$ transition of the *GMP-quadruplex*. This suggests an abrupt change in the columnar organization of the short intermolecular *TG_4T-quadruplex*, similar to the change in the columnar organization of the G-quartets at the $\Phi_{dc} \rightarrow \Phi_{oc}$ transition of the *GMP-quadruplex*. When this change in order is tuned by varying the osmotic pressure, we observe a much broader coexistence-region in the $\Phi_{dc} \rightarrow \Phi_{oc}$ transition for *TG_4T-quadruplex* than for the *GMP-quadruplex*. For clarity, in Fig. 2.4 we show the intercolumnar spacings for the *TG_4T-quadruplex* only at the upper and lower boundaries of the coexistence-region (inverted triangles). Intercolumnar spacings are about the same in the Φ_{oc} phases of the *TG_4T-quadruplex* and *GMP-quadruplex* arrays under the same pressure.

***Poly(AT*T)-triplex*:** *Poly(AT*T)-triplex* samples are prepared in the presence of 5 mM Mg^{2+}. The role of Mg^{2+} in the stability of DNA triplexes has been investigated [43], and stable *Poly(AT*T)-triplex* at [Mg^{2+}]=5 mM is reported. Under sufficient osmotic pressures in presence of 5 mM Mg^{2+}, *Poly(AT*T)-triplexes* self assemble into columnar hexagonal aggregates (see Chapter 5). Addition of 0.3 M K^+, while keeping [Mg^{2+}]=5 mM, causes the following changes in the *Poly(AT*T)-*

triplex arrays (under fixed pressure): (i) in the Φ_{oc} phase, expansion in the lateral direction (see Section 5.2 for details) and (ii) in the Φ_{dc} phase, destabilization of the *Poly(AT*T)-triplex*. The osmotic pressure required to prevent the destabilization of the *Poly(AT*T)-triplex* depends on the concentrations of K^+ and Mg^{2+}. At the $\Phi_{dc} \rightarrow \Phi_{oc}$ mesophase transition of the *Poly(AT*T)-triplex* $\left(\text{in the presence of 0.3 M } K^+ \text{ and 5 mM } Mg^{2+}\right)$ d_{int} changes from about 37Å to 33Å (Fig. 2.4). The changes were reversible for d_{int} less than ≈38Å. At larger spacings, once the *Poly(AT*T)-triplexes* disassociate, the triplex formation cannot be reestablished by simply increasing the osmotic pressure.

2.4 Discussion

Fiber diffraction data provide substantive evidence of helical stacking of the G-quartets [17] in *GMP-quadruplex* as well as of helical stacking of the base-pairs [16] in duplex DNA, at relative humidities corresponding to the osmotic pressures produced by the bathing PEG solutions that induced Φ_{oc} phases of these structures. These helical details are expected to be pronounced only in the presence of strong correlations between repeating units (base-pair for duplex and G-quartet for *GMP-quadruplex*) along the columnar axes. Additionally, the transitions occur when the intercolumnar spacings are comparable (see Table 2.1) to the helical pitch length. Based on this, one can argue that the helical nature of the base-stacking in DNA structures plays a key role in the $\Phi_{dc} \rightarrow \Phi_{oc}$ transitions of the DNA arrays. The formation of long-range translational and helical order along the columnar axis leads to long-range intercolumnar order in the Φ_{oc} phase.

We examined the $\Phi_{dc} \rightarrow \Phi_{oc}$ mesophase transitions of duplex, triplex, and quadruplex DNA structures. In particular, the spontaneous formations of highly-ordered G-quadruplex columns (*GMP-quadruplex* and *TG_4T-quadruplex*) under biologically relevant molecular crowding conditions are significant for their analogies with the

	a(nm)	λ(e/nm)	σ(e/nm^2)	P(nm)	$^{(\ddagger)}$Change in d_{int}	Δd_{int}(nm)	$^{(\dagger)}\Delta A_{cell}$(nm^2)	$^{(\#)}\Delta V_{pn}$(nm^3)
Duplex	1	6	0.95	3.4	≈3.7-to-3.5nm	0.19-0.21	0.11-0.12	0.19-0.20
*Poly(AT*T)-triplex*	1.04	9	1.38	3.4	≈3.7-to-3.3nm	0.35-0.40	0.19-0.22	0.22-0.24
GMP-quadruplex	1.25	12	1.53	4.1	≈4.2-to-3.5nm	0.65-0.70	0.43-0.46	0.36-0.39

Table 2.1. Quantitative information regarding the structure and the $\Phi_{dc} \rightarrow \Phi_{oc}$ transitions of duplex, *Poly(AT*T)-triplex*, and *GMP-quadruplex* DNA.
$^{(*)}$The structural parameters, effective radius (a) and helical pitch length (P), are from Ref. [17], [16], and [46].
$^{(\ddagger)}$These values are measured in 0.3 M K^+ solutions for duplex and *GMP-quadruplex*. These distances for duplex and *GMP-quadruplex* (comparable to pitch) decrease without a significant change in Δd_{int} with increasing K^+ concentration. The *Poly(AT*T)-triplex* measurements are carried out in the presence of 0.3 M K^+ and 5 mM Mg^{2+}. Lowering Mg^{2+} concentration any further (less than 5 mM), while keeping the K^+ concentration fixed at 0.3 M, results in the disassociation of the triplexes. Thus, the d_{int} values for the *Poly(AT*T)-triplex* that we report here (comparable to pitch) are near the biggest distances where the transition can be observed at [K^+]=0.3 M. See Section 5.1 and Section 5.2 for details.
$^{(\dagger)}$ A_{cell} is the hexagonal cross-sectional area surrounding the duplex, triplex, or *GMP-quadruplex*. ΔA_{cell} is the change in the *Wigner-Seitz cell* area at the transition.
$^{(\#)}$ ΔV_{pn} is the change in the volume per nucleotide at the transition. The change in the volume per stacking unit (i.e., base-pair for duplex, base-triplet for triplex, and G-quartet for *GMP-quadruplex*) is equal to ΔA_{cell} multiplied by the base-stacking height. We assumed that the base-stacking height (=0.34nm) is the same for all the structures and does not change at the transition. The overall uncertainty in the determination of ΔV_{pn} is about 10%.

stacking organization of G-quadruplex structures in the human telomere. A quasi-continuous helix that runs along the columnar axis by the stacking of G-quartets within the *TG_4T-quadruplex* columns [42] (similar to the helical stacking of the G-quartets in *GMP-quadruplex*) is possible with azimuthal rotations and arrangements of the *TG_4T-quadruplex blocks* relative to the adjacent *blocks*.

The formation of uniaxially ordered columnar liquid crystals has been observed also in the case of the stacking of very-short-fragment (6 base-pairs long) DNA duplexes [44]. This stacking behavior was explained by the end-to-end adhesion of the exposed hydrophobic cores of the short DNA segments. From the observed $\Phi_{dc} \rightarrow \Phi_{oc}$ first-order mesophase transition of the *TG_4T-quadruplex* arrays, as seen in the discon-

tinuous change in the x-ray diffraction patterns tuned by varying molecular crowding conditions, it is possible to argue that the high-planarity of the G-quartets in the *TG_4T-quadruplex* blocks makes the end-to-end stacking favorable. However, one could claim that the presence of the thymine bases at the ends of *TG_4T-quadruplex* blocks would likely weaken the stacking interactions and in turn make the uniaxial helical ordering unfavorable. The broad range of osmotic pressures where the phase coexistence is observed in *TG_4T-quadruplex* arrays (Fig. 2.5) might be attributed to the increased disorder due to the thymine bases at the ends.

In order to investigate the formation of ordered G-quadruplex columns in the telomere, the *22-mer HT-quadruplex* was specifically chosen for two reasons: (i) the four-repeat sequence $\mathrm{AG_3(TTAG_3)_3}$ is the likely candidate for the G-quadruplex formation *in vivo* and (ii) G-quadruplex conformation of this sequence under molecular crowding conditions is known. However, to the best of our knowledge, there is no direct evidence that the *22-mer HT-quadruplex* blocks would be organized into a columnar assembly in the non-crystalline state. At all osmotic pressures *unlinked 22-mer HT-quadruplex* blocks were observed to make only disordered columns, characterized by almost unchanged radial disorder (Fig. 2.5), implying also a pronounced stacking disorder. At large osmotic pressures it appears as if the disordered columns would have an effective diameter augmented by the contribution of the dangling TTA loops, while at small osmotic pressures the phosphate backbone connectivity of the *22-mer HT-quadruplex* blocks enhances their stability. The robust disordered columnar assembly would possibly be the outcome of the attenuated stacking interactions between the G-quartet cores of the *22-mer HT-quadruplex* blocks, compared with the very pronounced stacking interactions within the highly-ordered columnar phases of the *GMP-quadruplex* and the *TG_4T-quadruplex*. This preserves the fluid-like order in the *22-mer HT-quadruplex* columns at all crowding conditions.

Another feature of the ordered phases of the DNA structures is revealed by comparison of the characteristic decay lengths in the Π vs. d_{int} curves (Fig. 2.4) of duplex, triplex, and *GMP-quadruplex* DNA. In Chapter 1 we described the parametrization of the intercolumnar distance dependence of the osmotic pressure of the array in terms of a short-range hydration characteristic length and a longer-ranged Debye screening length. In the case of duplex DNA in monovalent salt solutions, at large separations in the ordered phase, the apparent decay length from the Π vs. d_{int} curve is close to the Debye length, suggesting that the electrostatic interactions dominate at these separations. When the surface-to-surface separation is smaller than about 7-8Å, the Π vs. d_{int} curves for all ionic concentrations converge to a single curve, suggesting also a universal short-range hydration repulsion that is independent of ionic strength. However, in the case of G-quadruplexes, neither the Debye length nor the expected characteristic length for the short-range hydration interactions (on the order of the size of a water molecule) are as anomalously small as the apparent lengths reported here ($\sim$1Å).

CHAPTER 3

THERMODYNAMICS & DETAILED DATA ANALYSIS

At the transition from the fluctuating phase to the condensed phase (where chain fluctuations are negligible) the order of packing, and thus the system entropy due to positional disorder, change significantly. This abrupt change in the nature of positional order is clearly evidenced in the x-ray diffraction radial intensity profiles (see Fig. 3.1). In addition, the sensitivity of the transition pressures to ionic strength suggests a change in net molecular charge at the transition. This change affects the strength of bare electrostatic interactions. Finally, helical interactions are expected to play a role in the condensed-phase packing and to reduce the net repulsion at the condensation transition.

The sensitivity of duplex DNA density to ionic strength (under a fixed external pressure Π_{ext}) is significantly enhanced near the hexatic−cholesteric transition. The apparent decay lengths in the osmotic pressure curves are close to the expected Debye lengths in the hexatic phase of duplex DNA near the transition. We discuss the method for estimating the changes in electrostatic interactions due to charge neutralization occurring at the transition (Section 3.2). We also investigate the sensitivity of the transition free energy to temperature (Section 3.3) in order to compute the entropy loss upon condensation.

The transition free energy per unit chain length is

$$\left(W/L\right)_{tr} = \Pi_{tr}\left(\Delta A\right)_{cell,tr} \tag{3.1}$$

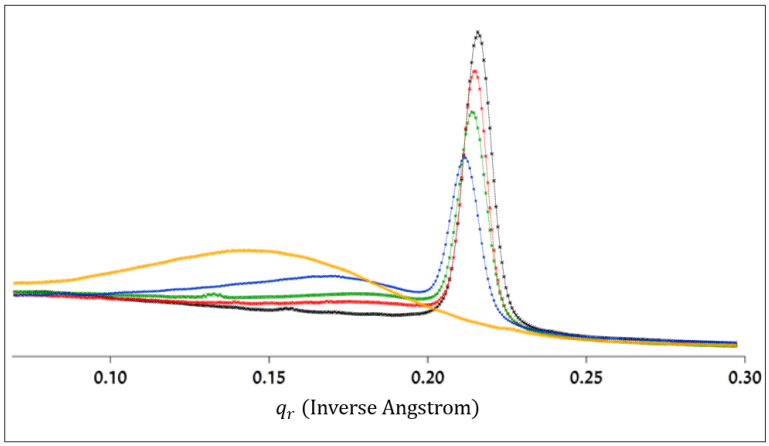

Figure 3.1. 1D intensity profiles (shown in a linear scale) from the *GMP-quadruplex* DNA sample, under different external pressures, showing the mesophase transition. Two distinct types of peaks coexist over a range of pressure. The transition is fairly sharp, and the integrated diffraction intensities (area under the peaks) from the same sample in the disordered and ordered phases are nearly the same.

where $\Delta A_{cell,tr}$ is the abrupt change in cell area as the DNA array is pushed through the cholesteric-to-hexatic (or the condensation) transition under the imposed osmotic pressure Π_{ext}=Π_{tr}. At the transition, the cylindrical cell radius changes abruptly from R=R_C^* to R=R_H^*, and the change in cell area is

$$\left(\Delta A\right)_{cell,tr} = \Delta\left(\pi R^2\right) = \pi\left[\left(R_H^*\right)^2 - \left(R_C^*\right)^2\right] = \pi\left[\left(R_H^* + R_C^*\right)\left(R_H^* - R_C^*\right)\right] .$$

For all [NaCl], the change in cell radius at the transition is about 1Å, i.e., R_H^*-R_C^* ≈-1Å. Using the measured values for R_H^* and R_C^* (Fig. 1.8) we find that the change in the cell area varies from ≈-120Å^2 (for [NaCl]=0.1M) to ≈-110Å^2 (for [NaCl]=0.4M) at the cholesteric-to-hexatic transition of duplex DNA. Therefore, the volume change per phosphate (calculated using the length per phosphate along the chain in the axial direction, i.e., 1.7Å) is ≈-190Å^3 to -200Å^3. The dependence of $\left(\Delta A\right)_{cell,tr}$ on [NaCl] is small, and the measured differences are nearly within our overall uncertainty (about 5%) in our experimental determination of $\left(\Delta A\right)_{cell,tr}$ by x-ray diffraction.

The transition pressure Π_{tr} and its ionic strength dependence can be measured with high accuracy using small temperature variations to finely tune the osmotic pressure (Chapter 5). For 0.1M $\leq$ [NaCl] $\leq$ 0.4M, Π_{tr} varies from $\approx$7.5 atm to $\approx$5.8 atm. The transition pressure (Π_{tr}) and the critical cell radii (R_C^* and R_H^*) , do not vary further for [NaCl] $\geq$ 0.4M. This is true only in the absence of polyvalent counterions such as $CoHex^{3+}$. Upon addition of $CoHex^{3+}$, the transition pressure is lowered.

3.1 Transition free energy and its components

The free energy change (per phosphate) at the transition is

$$W_{tr,pp} = \Pi_{tr}\big(\Delta V\big)_{tr,pp} \tag{3.2}$$

where $\big(\Delta V\big)_{tr,pp}$ is the volume change per phosphate ($\approx 200 \mathring{\mathrm{A}}^3$ for duplexes). When $\big(\Delta V\big)_{tr,pp}=200\mathring{\mathrm{A}}^3$ and Π_{tr}=6 atm,

$$\begin{aligned} W_{tr,pp} = \Pi_{tr}\big(\Delta V\big)_{tr,pp} &\approx (6\times 10^5 \mathrm{N/m^2})(2\times 10^{-28}\mathrm{m^3}) \\ &\approx 0.12\times 10^{-21}\mathrm{Joule} \approx 0.03 k_B\mathrm{T}. \end{aligned}$$

at T$\approx$300K. When [NaCl]=0.1M; $\Pi_{tr}\approx$7.5 atm, and the transition free energy is $W_{tr,pp}\approx 0.04 k_B$T. These energies, corresponding to $\approx 10-13\ k_B$T per persistence length of the duplex DNA, suggest that the free energy change at the transition cannot be explained solely by considering the abrupt change in positional disorder related to thermal chain fluctuations.

The transition free energy $W_{tr,pp}$ is decomposed into two parts:

$$W_{tr,pp} = \big(\Delta H\big)_{tr,pp} + \mathrm{T}\big(\Delta S\big)_{tr,pp} \tag{3.3}$$

The ΔS term is the change in entropy mostly due to the abrupt change in *configurational entropy* of the positional order at the transition. The ΔH term accounts for

non-entropic changes (i.e., changes in the bare interaction). At the transition, apart from the entropic change in positional order, the bare-interaction osmotic pressure (and the corresponding DNA free energy) also changes abruptly due to:

(i) a change of electrostatic repulsion due to charge neutralization at the transition;

(ii) interaction reduction due to helix re-arrangements at the cholesteric-to-hexatic transition.

The change in molecular surface charge due to counterion binding at the transition is discussed in Section 3.2.

3.2 Charge neutralization

The change in the effective molecular charge occurring at the transition due to counterion binding can be investigated by the sensitivity of the measured transition free energy per phosphate to the availability of neutralizing counterions via their bulk concentration:

$$\frac{\partial}{\partial \mu_S} W_{tr,pp} = \left(\Delta\Theta\right)_{tr,pp} \tag{3.4}$$

where $\left(\Delta\Theta\right)_{tr,pp}$ is the change in the fraction of bare surface charge neutralized by counterions at the transition, and μ_S is the chemical potential of the salt, i.e., $\mu_S = k_B\mathrm{T}\ \log[\mathrm{NaCl}]$. For duplex DNA the transition free energy (per phosphate) $W_{tr,pp}$ varies from 4% to 3% of $k_B\mathrm{T}$ upon varying [NaCl] from 0.1M to 0.3M, respectively (Section 3.1). From this dependence, by use of Eq. 3.4, we find $\left(\Delta\Theta\right)_{tr,pp}\approx 0.03$. For example, if Θ_{pp} changes from 0.50 to 0.47 for duplex DNA at a fixed ionic strength, then using $\xi_{e,0}=\Theta_{pp}-1$ the zeroth-order (n=0) term in the electrostatic part of the osmotic pressure changes by ≈10%. A change of Θ_{pp} from 0.70 to 0.67 would lead to ≈15% change in the repulsive electrostatic osmotic pressure. Therefore, the measured $(\Delta\Theta)_{pp}\approx 0.03$, when the *unknown* Θ_{pp} is varied in the range 0.5 to 0.7, leads to a change in magnitude of the electrostatic osmotic pressure near the transition of about 10 to 15%.

We proceed to the investigation of charge neutralization in the hexatic phase of duplex DNA. In particular, we investigate the sensitivity of [NaCl] to the free energy change upon changing the cell radius from $R{=}R_H^*$ (the largest cell radius in the hexatic phase) to $R{=}R_0$ (the smallest cell radius in the hexatic phase) where there is clearly discernible hexagonal symmetry in the x-ray diffraction patterns:

$$\left(W_{pp}\right)_{R_H^*\to R_0} = \int_{R_H^*}^{R_0} \Pi(R) d(\pi R^2)$$

and

$$\left(\Delta\Theta\right)_{hex,pp} = \frac{\partial}{\partial \mu_S}\left(W_{pp}\right)_{R_H^*\to R_0}$$

yields $\left(\Delta\Theta\right)_{hex,pp}{\approx}0.3$ independent of [NaCl]. For duplex DNA, $R_0{\approx}12$Å and at higher DNA densities the hexatic $\to$ orthorhombic transition ensues. In the *crystalline* orthorhombic phase, charge neutralization is expected to be complete, i.e., $\Theta_{pp}{=}1$, which suggests $\Theta_{pp}{\approx}0.70$ at the smallest DNA density in the hexatic phase where $R{=}R_H^*$.

On the other hand, by investigating the sensitivity of the DNA free energy to the ionic strength in the cholesteric phase, we find that Θ_{pp} varies with [NaCl]. Upon increasing the DNA density from effectively infinite dilution, where the interaxial separation is ≈50Å (for example the DNA density where there is no orientational ordering), up to the density at the cholesteric-to-hexatic transition, the change in Θ_{pp} is

$$\left(\Delta\Theta\right)_{chol,pp} \approx 0.8 - 0.3\log[\mathrm{NaCl}]$$

where [NaCl] is in mM units. This result suggests that $\left(\Delta\Theta\right)_{chol,pp}{\approx}20\%$ to 2% of the bare charge for [NaCl]=0.1M to 0.4M, respectively. Therefore, there is a detectable effect of [NaCl] on the change in the number of Na^+ ions adsorbed on the DNA surface as the chains are pushed to a density corresponding to $R{=}R_C^*$.

3.3 Entropy of the cholesteric packing

In order to quantify the entropy due to positional disorder in the *less-ordered* phase, we investigate the temperature sensitivity of the free energy change at the condensation transition. We calculate the entropy change per phosphate at the DNA condensation transition using the Clausius-Clapeyron relation. We start with $\left(\Delta W\right)_{tr,pp} = \left(\Delta H\right)_{tr,pp} + \mathrm{T}\left(\Delta S\right)_{tr,pp}$, so that

$$\frac{d(\Delta W)_{tr,pp}}{d\mathrm{T}} = \frac{d\left(\Delta H\right)_{tr,pp}}{d\mathrm{T}} + \left(\Delta S\right)_{tr,pp} . \tag{3.5}$$

The effect of temperature on $\left(\Delta H\right)_{tr,pp}$ is seen for the case of DNA condensation with Mn^{2+} ions [47]. We have also observed [10] *temperature-induced DNA condensation transitions* (where the DNA array is condensed with increasing temperature at fixed osmotic pressure) in the presence of $CoHex^{3+}$ when $[CoHex^{3+}]$ is close to the upper critical concentration. If we assume that the dependence of charge neutralization on temperature is negligible in the presence of only monovalent salts,

$$\left(\Delta S\right)_{tr,pp} \approx \frac{d(\Delta W)_{tr,pp}}{d\mathrm{T}} = -\left(\frac{d\Pi_{tr}}{d\mathrm{T}}\right)\left(\Delta V\right)_{tr,pp} \tag{3.6}$$

where $\left(\Delta V\right)_{tr,pp}$ is the volume change per phosphate at the transition and Π_{tr} is the transition osmotic pressure. $\left(\Delta V\right)_{tr,pp} \approx 200\text{Å}^3 - 360\text{Å}^3$ (independent of temperature variations in the range 15-45 °C) for duplex and *GMP-quadruplex* DNA, respectively. We were able to measure a slight dependence of Π_{tr} on temperature [10] through high-resolution control of the PEG osmotic pressure via its known temperature dependence. Temperature (in the range 15-45 °C) has no detectable effect on the DNA free energy for all DNA structures in the condensed phase.

For duplexes, the transition osmotic pressures (for $0.1\text{M} \leq [\text{NaCl}] \leq 0.4\text{M}$) vary by only ∼0.2 atm upon changing temperature from 15 to 45 °C. A linear fit to the measured Π_{tr} vs. transition temperature T_{tr} yields

$$\big(\Delta S\big)_{tr,pp} = \left(\frac{d\Pi_{tr}}{d\mathrm{T}_{tr}}\right)\big(\Delta V\big)_{tr,pp} \approx \frac{0.2 \text{ atm}}{30 \text{ K}} \times 200\text{Å}^3 \ .$$

At T=300 K,

$$\mathrm{T}\big(\Delta S\big)_{tr,pp} \approx 300 \text{ K}\left[\frac{0.2 \text{ atm}}{30 \text{ K}} \times 200\text{Å}^3\right] = 0.4 \text{ atm(nm)}^3 \approx 0.01 \ k_B\mathrm{T} \ ,$$

comparable to the fluctuational free energy F_{fl} per nucleotide near the transition (calculated in Section 1.4) when the scaling prefactor $c\approx1$ (Eq. 1.44). These results also suggest that the entropic part of the DNA nucleotide free energy change at the transition corresponds to $\sim1/3$ and $\sim1/4$ of the transition free energy, i.e, $W_{tr,pp} \approx 0.03 - 0.04 \ k_B\mathrm{T}$ (Section 3.1) at [NaCl]=0.4M and 0.1M, respectively.

3.4 Thermodynamics analysis of *GMP-quadruplex* DNA data

The volume change (per nucleotide) upon *GMP-quadruplex* condensation is approximately twice that for duplex DNA (see Table 2.1). In addition, at a fixed [NaCl] (for 0.1M $\leq$ [NaCl] $\leq$ 0.4M), the transition pressures are slightly larger for *GMP-quadruplex* DNA than for duplex DNA. For duplexes, upon increasing [NaCl] above 0.4M, the transition pressure does not vary further. However, for *GMP-quadruplexes* the transition pressure is lowered significantly by increasing [NaCl] to 1.0M (Fig. 3.2). Therefore, not only the volume change, but also the sensitivity of Π_{tr} to ionic strength is larger for *GMP-quadruplex* DNA than for duplex DNA. For *GMP-quadruplexes*, similarly to duplexes, $\big(\Delta V\big)_{tr,pp}$ is not sensitive to ionic strength.

The transition osmotic pressures vary from $\Pi_{tr}\approx$9.5 atm to 3.9 atm upon increasing the monovalent-salt concentration (at a fixed temperature) from 0.15M to 1M, respectively. The corresponding transition free energies for *GMP-quadruplexes*, calculated using Eq. 3.2 and $\big(\Delta V\big)_{tr,pp}\approx$360Å , vary approximately linearly from $W_{tr,pp}\approx3.5$

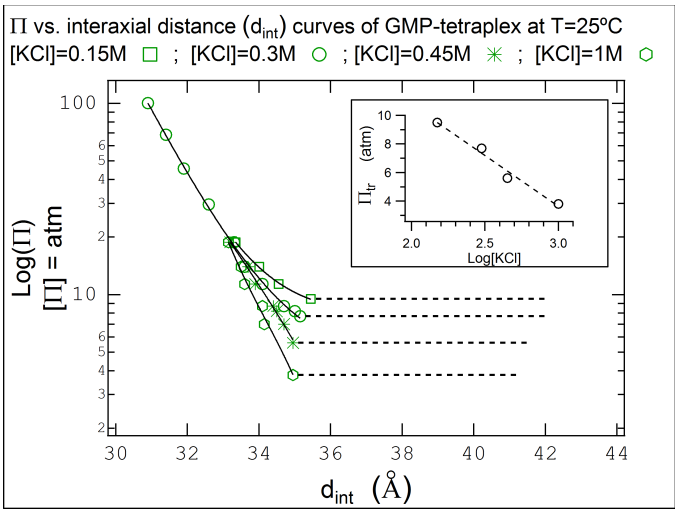

Figure 3.2. Solid lines are exponential or polynomial fits as guides to the eye. Horizontal dashed lines show the transitions to the fluctuating phase. Data are shown for [KCl]=0.15, 0.45, 1M up to the pressure ($\Pi \approx 20$ atm) where the osmotic pressure curves for all [KCl] converge. **Inset:** Transition pressure Π_{tr} vs. Log[KCl] where [KCl] is in mM units and a linear fit to the data.

to 1.5 atm(nm)^3. For *GMP-quadruplexes*, from this dependence, using Eq. 3.4 and the relation $\mu_S = k_B\mathrm{T}\ \log[\mathrm{KCl}]$, we find

$$\left(\Delta\Theta\right)_{tr,pp} \approx \frac{2\ \mathrm{atm(nm)}^3}{k_B\mathrm{T}\Big(\log[1000] - \log[150]\Big)} \approx \frac{0.05\ k_B\mathrm{T}}{0.82\ k_B\mathrm{T}} \approx 0.06\ ,$$

which is approximately twice as large as the fractional charge neutralization upon condensing duplex DNA (3%) with monovalent salts in the absence of polyvalent salt. At pressures greater than the transition pressure, *GMP-quadruplex* osmotic-pressure curves for all [NaCl] converge to a single curve, meaning the sensitivity of the *GMP-quadruplex* DNA density to ionic strength (at a fixed pressure) is negligible (Fig. 3.2). This observation leads us to suspect that either:

(i) Complete neutralization is achieved upon compressing the condensed array to a slightly higher density than the transition density; or

(ii) Counterion localizations in the center of the chains (as evidenced in the x-ray crystallography) considerably modify the interaction potentials.

The dependence of the transition osmotic pressure on temperature is more pronounced for *GMP-quadruplexes* than for duplexes. For *GMP-quadruplexes*, Π_{tr} increases by about 0.4 atm upon increasing the temperature from 15 to 45 °C at [KCl]=0.3M. The dependence of Π_{tr} on T_{tr} is approximately linear. A linear fit yields

$$\begin{aligned} \mathrm{T}\big(\Delta S\big)_{tr,pp} &= \mathrm{T}\left[\left(\frac{d\Pi_{tr}}{d\mathrm{T}_{tr}}\right)\big(\Delta V\big)_{tr,pp}\right] \approx 300\ \mathrm{K}\left[\frac{0.4\mathrm{atm}}{30\ \mathrm{K}} \times 360\mathring{\mathrm{A}}^3\right] \\ &\approx 1.4\ \mathrm{atm(nm)}^3 \approx 0.035\ k_B\mathrm{T}\ , \end{aligned}$$

which corresponds to a major portion (approximately 50%) of the total transition free energy (i.e., $W_{tr,pp}$≈2.7 atm(nm)^3≈0.07 k_BT for *GMP-quadruplex* DNA) at [KCl]=0.3M. In addition, the transition entropy is ≈3-4 times larger for *GMP-quadruplex* DNA than for duplex DNA for [NaCl] and [KCl] between 0.1M and 0.45M.

CHAPTER 4

CONCLUSIONS AND FUTURE DIRECTIONS

We showed and analyzed how solution osmotic pressure controls DNA density, the related molecular order, and the phase transitions between differently ordered DNA-analogue arrays. We proposed that the *effective attractions* occurring at the condensation transitions of DNA structures can be decomposed into two components:
(i) Diminished repulsion, due to suppressed chain fluctuations at the transition.
(ii) Diminished repulsive bare interactions, due to the induced azimuthal ordering of DNA helices at the transition.
Parts (i) and (ii) are related to the elastic and helical properties, respectively, of a particular DNA structure.

The free energies of DNA structures in the condensed and fluctuating phases (as well as the free energy change at the transition between these two phases) are related to their helical and elastic properties. The repeating units along the columnar (or molecular) axes of the DNA structures are constrained by (i) the base-stacking interactions and (ii) the sugar-phosphate links between the adjacent units. In the condensed phases, DNA structures are packed strictly, and molecular motions are suppressed; thus elastic properties of the molecules do not play a role in the interactions. Therefore, the study of positional disorder in the fluctuating phases of DNA structures is important in order to understand the relative contributions of (i) and (ii) to molecular stability. The entropy due to positional disorder can be quantified by investigation of x-ray diffraction peak-widths in the fluctuating phases, as well as temperature sensitivity of the transition free energy.

The nature of the extremely short-range interactions (with an exponential decay length ∼1Å) observed in the ordered G-quadruplex arrays remains to be elucidated. This finding points to the implied relation between helicity and the osmotic-pressure dependence of density in the condensed DNA phases. It is also possible that the counterion localization within four-strand DNA structures act differently than bare surface charge neutralization seen in the case of duplex DNA. In this case, the localized positive ions modify the electric field around the molecule (which is due to the phosphates on the molecular surface) and thus modify the interaction potential. The decay length of the measured osmotic pressure vs. interaxial distance curve for *GMP-quadruplex* DNA is significantly smaller than the Debye length, suggesting that the osmotic pressure determined by the zeroth-order cylinder term in the interaction potential is suppressed. This effect can be explored via the linearized Poisson-Boltzmann equation for a cylinder concentric with another oppositely charged thin cylinder or line charge.

The positional disorder in the Φ_{dc} phase is more pronounced in the *GMP-quadruplex* arrays than in the duplex, *22-mer HT-quadruplex*, and TG_4T*-quadruplex* arrays (Fig. 2.5). The data point to the increased molecular stability by the sugar-phosphate backbone in duplex, *22-mer HT-quadruplex*, and TG_4T*-quadruplex* relative to the *GMP-quadruplex*. Nonetheless, the base-stacking interactions between the G-quartets are obviously strong enough and lead to the formation of disordered *GMP-quadruplex* columns at osmotic pressures as low as ≈3-4 atm (corresponding to ≈15 wt% PEG 8000 concentration). On the other hand, in the condensed phase, *GMP-quadruplexes* are stiffer than duplex DNA. Their azimuthal 4-fold symmetry allows stricter packing, as seen in the Lorentzian x-ray diffraction peak widths (Fig. 2.5).

To sum up, the nature of the condensation transition is the same for both canonical duplex DNA and nancanonical DNA-analogues, but we showed that the transition free energy and entropy are larger for G-quadruplex DNA than for duplex DNA. By

these observations, one should expect that:

(i) in the less-ordered phase the repulsion due to chain fluctuations is much larger for G-quadruplexes than for duplexes;

(ii) the lowering of free energy induced by azimuthal orientation of the chains (due to helical interactions) at the mesophase transition is larger for G-quadruplexes than for duplexes.

It is inevitable that changes in positional order and azimuthal order in DNA phases occur concurrently. To account for an abrupt change in the electrostatic part of the free energy at the transition,

(iii) counterion localization and charge neutralization must also be considered.

CHAPTER 5

EXPERIMENTAL METHODS

5.1 Sample preparations

DNA oligonucleotide samples were ordered from Integrated DNA Technologies and were stored in a freezer until the time of measurements. Below we describe the methods of preparations of each DNA structure considered in this thesis.

Poly(AT*T)-triplex: *Poly(AT*T)-triplex* structures are made of 50 bases long Poly(A) and Poly(T) sequences, by heating the solutions of Poly(A) and Poly(T) (mixed at 1:2 ratio) to 90 °C and slowly cooling to room temperature. The oligonucleotide concentration in the annealing solution (containing 5 mM Mg^{2+}) was ∼0.1 mg/ml. Following the annealing, we measured the CD spectra of the samples to ensure that the *Poly(AT*T)-triplexes* were formed (see Section 5.3). We then concentrated the *Poly(AT*T)-triplex* solution to about 1 mg/ml oligonucleotide concentration.

The *Poly(AT*T)-triplex* arrays are formed in PEG 8000 solutions: We mixed 1 ml samples of the 1 mg/ml *Poly(AT*T)-triplex* solution with 1 ml 50 wt% PEG 8000 (both containing 5 mM Mg^{2+}). Thus the final solution contained ∼1 mg of *Poly(AT*T)-triplex* under 25 wt% PEG 8000. Self-aggregated *Poly(AT*T)-triplex* arrays are equilibrated in the 25 wt% PEG 8000 solutions for about 48 hours and then collected by centrifuging for ∼20 hours at 4 °C and 30,000g. We then transferred the collected pellets into large volumes (∼5 ml) of PEG 8000 bathing solutions at various wt% concentrations (also containing the desired ionic conditions, i.e., 5 mM Mg^{2+} and 0.3 M K^{+}). We performed the x-ray diffraction measurements after equilibrating the *Poly(AT*T)-triplex* arrays in the bathing solutions for about 48 hours.

22-mer HT-quadruplex: Quadruplexes were formed by heating the four-repeat telomeric sequence $AG_3(TTAG_3)_3$ solution at 95 °C and [KCl]=50 mM for 5 min and then cooling to room temperature. The oligonucleotide concentration in the annealing solution was ∼0.1 mg/ml. We measured the CD spectra of the samples to ensure the formation of the structure (see Section 5.3). We then equilibrated the quadruplexes in PEG 8000 solutions (40 wt%). The structural conversion of the $AG_3(TTAG_3)_3$ sequence to parallel-stranded *22-mer HT-quadruplex* conformation in PEG solutions was seen [32, 33].

22-mer HT-quadruplex arrays aggregated in the 40 wt% PEG 8000 solutions were collected by centrifugation. The concentrated pellet was then transferred into new solutions of PEG 8000 (at various wt% concentrations) and [KCl]=0.3 M for equilibration (∼48 hours). Before the x-ray diffraction experiments, the solutions were centrifuged for long hours (∼20-30 hours) at 4 °C and 30,000g. The pellets (∼1 mg of weight) were held under the same solution conditions (0.3 M K^+ and the desired PEG wt%) during the diffraction measurements.

GMP-quadruplex: We prepared the GMP solutions (1 mg/ml) at [KCl]=0.3 M with stirring at room temperature for about 2-3 hours. We then mixed 1 ml samples of the prepared GMP-solution with 4 ml 25 wt% PEG 8000 solutions (containing 0.3 M K^+), i.e., the final solution contains ∼1 mg of GMP under 20 wt% PEG 8000 and 0.3 M K^+. Under these conditions, GMP precipitates and pellets are formed by centrifugation. We transferred the collected pellets into new PEG 8000 solutions (at various wt% concentrations) for the x-ray diffraction experiments.

TG_4T-quadruplex: Quadruplex formation was induced by heating TG_4T oligonucleotide solution at 80 °C for 5 min and then cooling to room temperature at [KCl]=0.1 M. The oligonucleotide concentration in the annealing solution was ∼0.1 mg/ml. *TG_4T-quadruplex* is extensively studied in the literature. Their conformation

in K^+ solutions is well-known [4]. We measured the CD spectra of the TG_4T oligonucleotide solutions before and after the heat incubation to confirm parallel-stranded intermolecular *TG_4T-quadruplex* formation (see Section 5.3).

Unoriented duplex DNA: Long-fragment DNA was purchased from Sigma-Aldrich Corporation and used without further purification. The unoriented duplex DNA samples are prepared using the described method [8, 10].

Oriented duplex DNA: Oriented DNA samples were prepared at the Institut Laue Langevin (Grenoble, France) using the described setup and procedure [51].

5.2 *Poly(AT*T)-triplex* mesophase transitions and stability in K^+ solutions

We prepared Poly(AT*T) DNA triplexes in the presence of Mg^{2+}. Triplex arrays are first formed and equilibrated for 48 hours in 25 wt% PEG 8000 solutions in the presence of 5 mM Mg^{2+} only. The measured ordering transition of the *Poly(AT*T)-triplex* is shown below in Fig. 5.1.

When K^+ is added to the *Poly(AT*T)-triplex* solution while keeping the $[Mg^{2+}]$ fixed, interaxial separation d_{int} increases in both mesophases. The osmotic pressure required for the ordering transition strongly depends on the $[Mg^{2+}]/[K^+]$ ratio. In Fig. 5.1 the transitions at $[Mg^{2+}]$=5 mM in the presence (0.3 M) and absence of KCl are displayed.

While the interaxial separation in the *Poly(AT*T)-triplex* arrays increases upon addition of K^+, the triplexes are also destabilized at larger separations. At [KCl]=0.3 M, *Poly(AT*T)-triplexes* disassociate when d_{int} is larger than 38Å. The changes in the triplex arrays at the mesophase transition are not reversible once the triplexes disassociate.

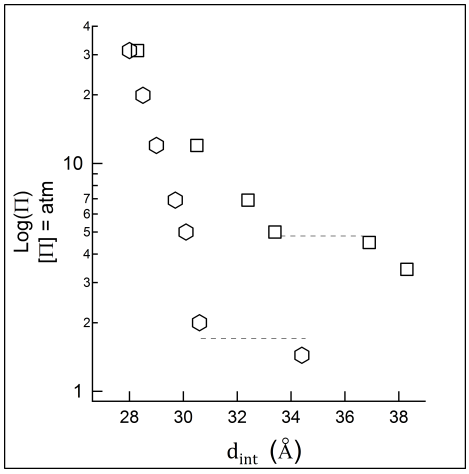

Figure 5.1. *Poly(AT*T)-triplex* mesophase transitions at two different bathing solution conditions. Hexagon: [MgCl]=5 mM only, [KCl]=0. Square: [MgCl]=5 mM and [KCl]=0.3 M.

5.3 DNA structure characterization - CD spectra

In this section we describe the methods of characterizations of the *22-mer HT-quadruplex*, the *TG_4T-quadruplex*, and the *Poly(AT*T)-triplex*. We compare our obtained CD spectra of these DNA structures with spectra in the literature [4, 48–50] and confirm their conformations in solution. The measured CD spectra are shown in Fig. 5.2.

The annealing solution conditions for the *22-mer HT-quadruplex*, the *TG_4T-quadruplex*, and the *Poly(AT*T)-triplex* were described in detail in Section 5.1. Briefly here, *22-mer HT-quadruplexes* and *TG_4T-quadruplexes* were formed in the presence of KCl (50 mM and 100 mM, respectively) only. The annealing solution for the *Poly(AT*T)-triplexes* contained 5 mM $MgCl_2$ only. Oligonucleotide concentrations in the annealing solutions were fixed at ∼0.1 mg/ml for all the structures. The CD spectra are measured following the annealing.

The samples of the triplex and quadruplex DNA structures that we prepared at the UMass Amherst Physics Department (using the protocols described in Section 5.1) were sent to the School of Medicine at Case Western Reserve University, where CD

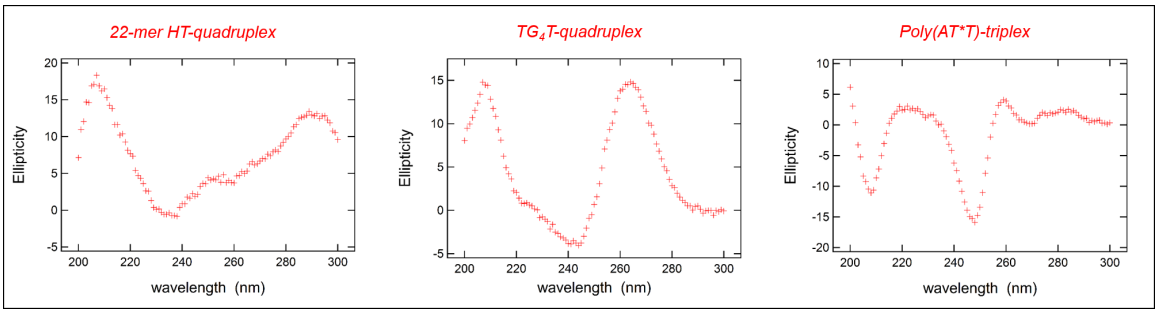

Figure 5.2. Measured CD spectra of the *22-mer HT-quadruplex* (left), *TG_4T-quadruplex* (middle), and *Poly(AT*T)-triplex* (right). The oligonucleotide concentration was ∼0.1 mg/ml for all the structures. The ionic conditions are described in Section 5.1.

spectra measurements were performed using the Circular Dichrosim Spectrometer (AVIV) for DNA-structure characterization (see Fig. 5.2). X-ray diffraction measurements were carried out at the UMass Amherst Physics Department. Following annealing, the triplex and quadruplex DNA structures were transferred into various solutions with the desired ionic and molecular crowding conditions (see Section 5.1) for the x-ray diffraction experiments.

5.4 X-ray diffraction data analysis

X-ray diffraction measurements are made using the in-house setup at the UMass Amherst Physics Department (see Section 5.6). Brief explanations of the x-ray diffraction data analysis are given in the caption to Fig. 2.3. In this section we describe the obtained radial intensity distributions and their fittings in detail.

For data centering and extracting 1D diffraction intensity distributions from 2D images, *SAXSGUI* (from Rigaku) is used. Intensity profiles (shown in a linear scale in Fig. 5.3) are calculated by radial integration of the intensity distributions in the 2D raw x-ray diffraction images. The radial component of the scattering wave vector (q_r) is calculated from

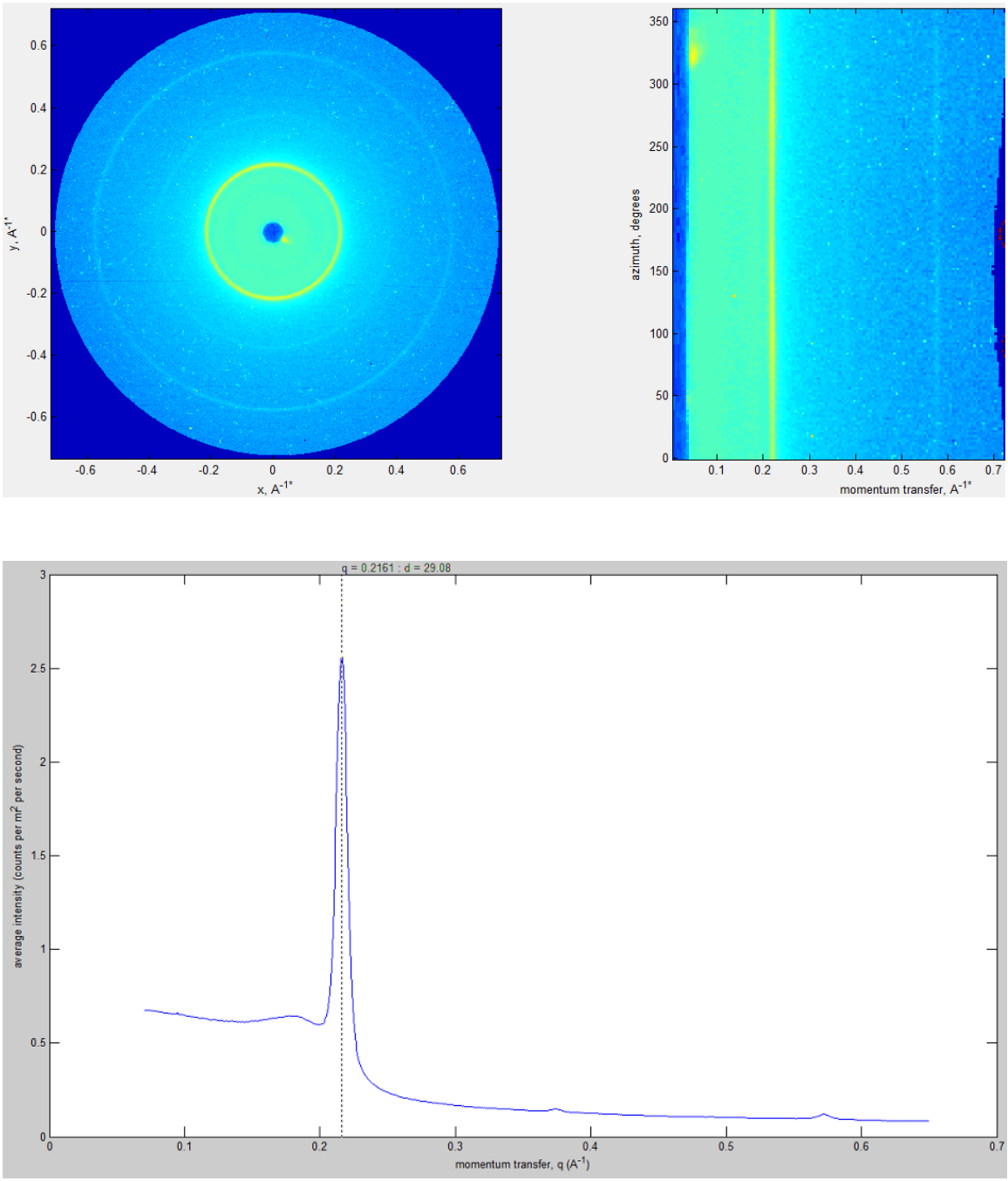

Figure 5.3. Top left: Typical 2D raw x-ray image obtained using in-house setup at the UMass Amherst Physics Department (see Section 5.6). **Top right:** Azimuthal angle vs. radial component of the momentum transfer (q_r) obtained using *SAXSGUI* software. **Bottom:** Intensity vs. q_r obtained by radial integration. Higher-order diffraction peaks confirm hexagonal packing. The broad Gaussian superimposed with the sharp Lorentzian first-order diffraction peak is due to phase-coexistence in this particular sample. See Fig. 2.3 for details.

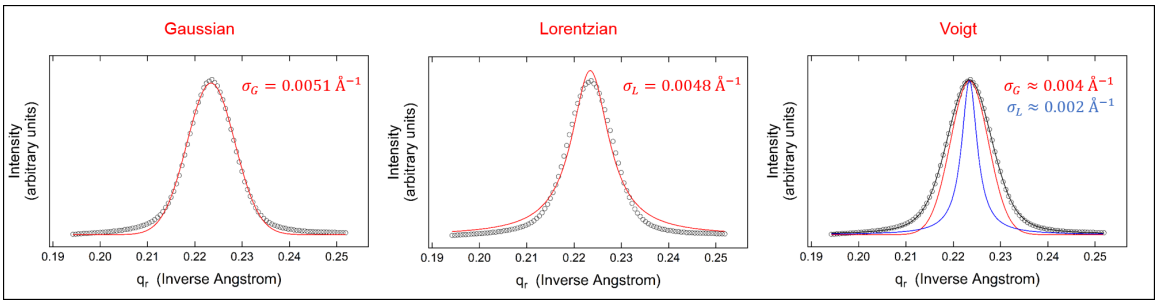

Figure 5.4. The fits of the ordered columnar DNA phase diffraction peaks to a Gaussian (left), a Lorentzian (middle), and the Voigt (right) function. The latter (convolution of a Gaussian and a Lorentzian) describes the shape of the peak. Here, the Gaussian (red in the right panel) is due to instrumental broadening. The Lorentzian (blue in the right panel) is due to the long-range nature of positional order. The correlation length in the ordered columnar phase is equal to the inverse of the FWHM of the Lorentzian, which is calculated using Eq. 5.7 above.

$$q_r{=}(4\pi/\lambda)sin(\theta/2)\ , \tag{5.1}$$

where θ is scattering angle and λ is x-ray wavelength. The interaxial spacings (d_{int}) are determined from the peak positions (q_0) and assumed hexagonal packing symmetry as

$$d_{int}{=}\big(2/\sqrt{3}\big)d_{Bragg}\ , \tag{5.2}$$

where $d_{Bragg}{=}2\pi/q_0$.

Sharp diffraction peaks in the condensed phases are fitted to a Lorentzian convolved with a Gaussian (in order to take into account instrumental broadening) after background subtraction (Fig. 5.4). The Gaussian and the Lorentzian are described as

$$G(q, q_0, \sigma_G) = A \times Exp\left[-\frac{1}{2}\Big(\frac{q-q_0}{\sigma_G}\Big)^2 \right] \tag{5.3}$$

and

$$L(q, q_0, \sigma_L) = \frac{B}{(q-q_0)^2 + \sigma_L^2} \tag{5.4}$$

respectively. In Fig. 5.4 we illustrate the fits of the ordered columnar phase diffraction peak to a Gaussian, a Lorentzian, and the convolution of Gaussian with a Lorentzian.

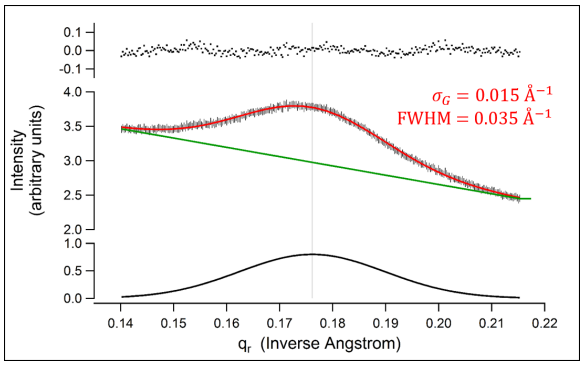

Figure 5.5. The fitting of the broad Gaussian-shaped x-ray diffraction peak in the fluctuating DNA mesophase. Gaussian broadening and the corresponding FWHM (given in Fig. 2.5), due to positional disorder in the hexagonal array, are calculated as $\sigma_G = 0.015$ Å^{-1} - 0.004 Å^{-1} = 0.011 Å^{-1} and FWHM = $2\sqrt{2\ln 2}\ \sigma_G \approx 0.025$ Å^{-1}. We subtract 0.004Å^{-1} from σ_G in order to take into account instrumental broadening. See Fig. 5.4 for the determination of the effect of instrumental broadening on the diffraction peak widths. See also Section 5.6 for the determination of instrumental broadening from the analysis of the direct x-ray beam shape.

The latter is called the Voigt function,

$$V(q, q_0, \sigma_L) = G(q, q_0, \sigma_G) * L(q, q_0, \sigma_L)\ . \tag{5.5}$$

The diffraction peaks in the ordered columnar DNA phases are described best by the Voigt function when $\sigma_G = 0.004$Å^{-1} (see also Section 5.6 for the determination of instrumental broadening from the analysis of the direct x-ray beam shape.). Broad diffraction peaks in the disordered columnar DNA phases are Gaussian-shaped and fitted to $G(q, q_0, \sigma_G)$. The radial disorder in the disordered columnar DNA arrays leads to Gaussian broadening of the diffraction peaks around average momentum transfer q_0 (which is related to the average distance between the molecules). In this case we take into account the effect of instrumental broadening by subtracting the 0.004Å^{-1} from the σ_G value found from the fit (see Fig. 5.4).

The FWHM given in Fig. 2.5 are then calculated as

$$\text{FWHM} = 2\sqrt{2\ln 2}\ \sigma_G \tag{5.6}$$

and

$$\text{FWHM} = 2\ \sigma_L \tag{5.7}$$

for the disordered and the ordered columnar DNA phases, respectively.

5.5 PEG 8000 osmolality, its polymer/solution weight ratio and temperature dependencies, and PEG 8000 osmolality in the presence of salt ions in the solution

In the osmotic stress experiments and the mesophase transition measurements, DNA samples are equilibrated against PEG 8000 solutions of different polymer/solution weight ratio c_P (i.e., the ratio of the weight of PEG 8000 in the solution to the total weight of the solution). PEG 8000 is purchased from Sigma-Aldrich Corporation and used without further purification. PEG 8000 solution osmotic pressures (Π), as a function of c_P and temperature, measured by membrane osmometry, are given in Fig. 5.6. The osmotic pressure of PEG, as well as the temperature dependence of the osmotic pressure of PEG, are not new. They have been reproduced by a variety of experimental methods (e.g., vapor pressure osmometry, membrane osmometry).

For the neutral flexible polymer solutions [52], the osmotic pressure in the semidilute regime is described with the des Cloizeaux limiting form, i.e., $\Pi \sim c_P^{9/4}$. PEG 8000 is a neutral flexible polymer. Its concentrations used in this study to produce osmotic pressures are in the semidilute regime [52]. The fittings of the PEG 8000 osmotic pressure data (Π vs. c_P) to the $c_P^{9/4}$ scaling form are shown in Fig. 5.7 (left panel) for different temperatures. Π as a function of c_P (at constant T) are extracted from the fits.

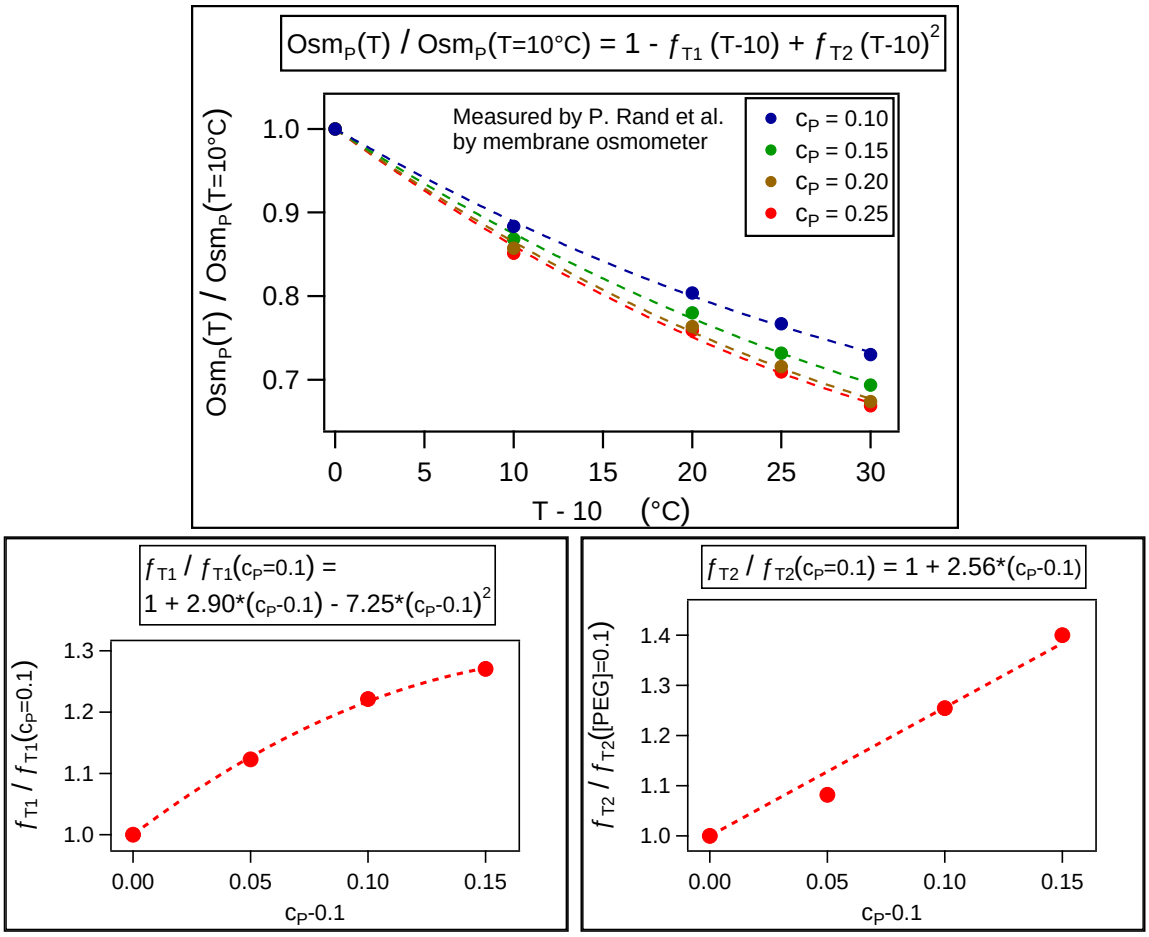

Figure 5.6. Temperature-dependent osmotic pressure data of PEG 8000 solutions, from Ref. [7]. For each polymer/solution weight ratio (c_P), osmotic pressure Π varies almost linearly with temperature (decreases with increasing T) when 20 °C $\leq$ T $\leq$40 °C. Π as a function of T (at constant c_P) are extracted from parabolic fits.

Finally, PEG 8000 osmotic pressures are not corrected for the effect of salt on PEG 8000 activity. We include, however, the osmolalities of PEG 8000 and salt mixtures in water, as measured with vapor pressure osmometer (see right panel in Fig. 5.7).

Osmolality measurements can be converted to osmotic pressures (Π) in units of atm using the formula

$$\Pi = \mathrm{RT}c \ ,$$

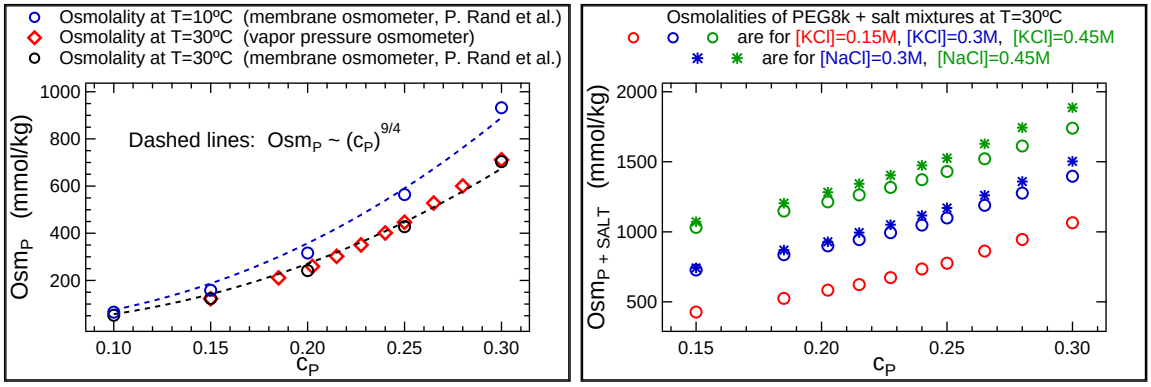

Figure 5.7. Left: PEG 8000 osmolality vs. c_P as measured with vapor pressure osmometer at T=30 °C (red square) and with membrane osmometer at T=10 °C (blue circle) and T=30 °C (black circle). Blue and black dashed lines represent the fittings of the data to the $c_P^{9/4}$ scaling form for T=10 °C and T=30 °C, respectively. **Right:** Osmolalities of PEG 8000 and salt mixtures, as measured by vapor pressure osmometer, as a function of c_P for various [NaCl] and [KCl].

where c =osmolality in moles/kg, when RT≈23.5 kg.atm/mol and ≈25.2 kg.atm/mol at T=10 °C and T=30 °C, respectively. Finally, for osmolalities of NaCl and KCl solutions (in the absence of PEG), see Ref. [53].

5.6 X-ray diffraction setup

DNA pellets are transferred into sample cells for x-ray measurements and the sample cells are sealed against evaporation. MicroMax-002+ x-ray generator from Rigaku with a microfocus sealed tube x-ray source is used in the measurements. The optic module with multilayer reflectors is designed by Rigaku based on the need of our experiments. MicroMax-002+ combined with the optical system leads to a beam of monochromatic radiation (wavelength λ=1.54 Å and focus at ∼400 mm from the end of optic module). The x-ray slit from Huber Diffraktionstechnik is used to shield the background scatter and to control the size of the beam. After passing the slit, the beam of about 0.6 mm diameter enters the sample and detector chamber.

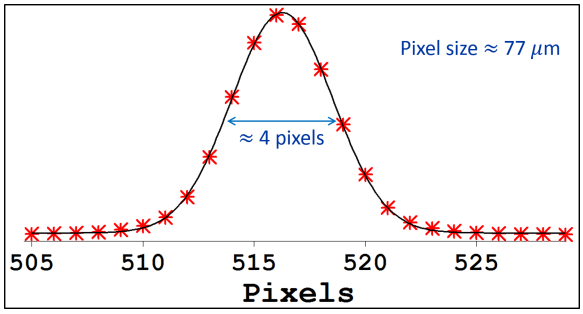

Figure 5.8. Radial intensity profile of the x-ray beam used in x-ray diffraction peak measurements, explained in Section 5.4: The width of the Gaussian describing the radial intensity distribution of the incident x-ray beam cross-section on the detector surface is ≈0.3 mm. This effect (called "instrumental broadening") is taken into account in the x-ray diffraction peak fittings and when calculating the standard deviation of the momentum transfer in the radial direction (q_r).

2D X-ray images are taken with a Rigaku Mercury-3 CCD X-ray detector (75 mm diameter circular image area and ∼75 μm pixel size). The sample-to-detector distance is ∼200 mm. The angular range of x-ray scattering covers a wave vector range from 0.05Å^{-1} to 0.75Å^{-1} in which q_r=$(4\pi/\lambda)sin(\theta/2)$, where θ is the scattering angle.

Samples are exposed to an x-ray beam having a well-defined steady Gaussian shape, and the resolution is increased by long data-collection times. In Fig. 5.8 we show the cross-section of the incident x-ray beam used in this study. Additionally, in Section 5.4 we described the method to deconvolute the Gaussian beam function (determined from the beam shape) from the measured diffraction peaks to account for instrumental broadening.

The width of the Gaussian describing the radial intensity distribution of the incident x-ray beam cross-section on the detector surface is ≈0.3 mm, which corresponds to $\theta/2 \approx 0.3^\circ$ when the sample-to-detector distance is ∼220 mm. Using Eq. 5.1 and the x-ray wavelength $\lambda = 1.54$ Å, we find the corresponding broadening in the intensity vs. q_r diffraction peaks as

$$\sigma_{beam}=(4\pi/1.54\ \text{Å})sin(0.3) \approx 0.004\ \text{Å}^{-1}.$$

BIBLIOGRAPHY

[1] Bloomfield, V.A., et al. *Nucleic Acids: Structures, Properties, and Functions* (University Science Books, 2000).

[2] Malvy, C., Harel-Bellan A. & Pritchard L.L. *Triple Helix Forming Oligonucleotides* (Kluwer Academic Publishers, Boston, 1999).

[3] Spindler, L. & Fritzsche, W. *Guanine Quartets: Structure and Application* (RSC Publishing, 2012).

[4] Neidle, S. & Balasubramanian, S. *Quadruplex Nucleic Acids* (RSC Publishing, 2006).

[5] Rey, A.D. Liquid crystal models of biological materials and processes. *Soft Matter* **6,** 3402-3429 (2010).

[6] Podgornik, R., et al. Bond orientational order, molecular motion, and free energy of high-density DNA mesophases. *Proc. Natl. Acad. Sci. USA* **93,** 4261-4266 (1996).

[7] Parsegian, V.A., Rand, R.P., Fuller, N.L. & Rau, D.C., Osmotic stress for the direct measurement of intermolecular forces. *Meth. Enzym.* **127,** 400-416 (1986).

[8] Rau, D.C. & Parsegian, V.A. Direct measurement of the intermolecular forces between counterion-condensed DNA double helices. Evidence for long-range attractive hydration forces. *Biophys. J.* **61,** 246-259 (1992).

[9] Stanley, C. & Rau, D.C. Evidence for water structuring forces between surfaces. *Curr. Opin. Colloid Interface Sci.* **16,** 551-556 (2011).

[10] Yasar, S., et al. Continuity of states between the cholesteric−line hexatic transition and the condensation transition in DNA solutions. *Scientific Reports*, **4,** 6877 (2014).

[11] Kornyshev, A.A. & Leikin, S. Theory of interaction between helical molecules. *Rev. Mod. Phys.* **79,** 943-996 (2007).

[12] Grønbech-Jensen, N., Mashl, R.J., Bruinsma, R.F. & Gelbart, W.M. Counterion-induced attraction between rigid polyelectrolytes. *Phys. Rev. Lett.* **78,** 2477 (1997).

[13] Qiu, X., et al. Inter-DNA attraction mediated by divalent counterions. *Phys. Rev. Lett.* **99,** 038104 (2007).

[14] Bloomfield, V.A. DNA condensation. *Curr. Opin. Struc. Biol.* **6,** 334-341 (1996).

[15] Besteman, K., Van Eijk, K. & Lemay, S.G. Charge inversion accompanies DNA condensation by multivalent ions. , *Nature Phys.* **3,** 641-644 (2007).

[16] Zimmerman, S.B. & Pheiffer, B.H. Helical parameters of DNA do not change when DNA fibers are wetted: X-ray diffraction study. *Proc. Natl. Acad. Sci. USA* **76,** 2703-2707 (1979).

[17] Zimmerman, S.B. X-ray study by fiber diffraction methods of a self-aggregate of Guanosine-5'-Phosphate with the same helical parameters as Poly(rG). *J. Mol. Biol.* **106,** 663-672 (1976).

[18] Kornyshev, A.A., et al. Direct observation of azimuthal correlations between DNA in hydrated aggregates. *Phys. Rev. Lett.* **95,** 148102 (2005).

[19] Chaikin, P.M. & Lubensky, T.C. *Principles of Condensed Matter Physics* (Cambridge University Press, Cambridge, 1995).

[20] Lorman, V., Podgornik, R. & Žekš B. Positional, reorientational, and bond orientational order in DNA mesophases. *Phys. Rev. Lett.* **87**, 218101 (2001).

[21] Strey, H.H., et al. Refusing to twist: Demonstration of a line hexatic phase in DNA liquid crystals. *Phys. Rev. Lett.* **84,** 3105-3108 (2000).

[22] Fuoss, R., Katchalsky, A. & Lifson, S. The potential of an infinite rod-like molecule and the distribution of the counterions. *Proc. Natl. Acad. Sci. USA* **37,** 579-589 (1951).

[23] Debye, P. & Hückel, E. The theory of electrolytes I. The lowering of the freezing point and related occurrences. *Physik. Z.* **24,** 185-206 (1923).

[24] Vainshtein, B.K. *Diffraction of X-ray by Chain Molecules* (Elsevier, Amsterdam, 1966).

[25] Marčelja, S. & Radić, N. Repulsion of interfaces due to boundary water. *Chem. Phys. Lett.* **42,** 129-130 (1976).

[26] Leikin, S., Parsegian, V.A., Rau, D.C. & Rand, R.P. Hydration Forces. *Annu. Rev. Phys. Chem.* **44,** 369-395 (1993).

[27] Strey, H.H., Parsegian, V.A. & Podgornik, R. Equation of state for polymer liquid crystals: Theory and experiment. *Phys. Rev. E* **59,** 999-1008 (1999).

[28] Baumann, C.G., Smith, S.B., Bloomfield, V.A. & Bustamante, C. Ionic effects on the elasticity of single DNA molecules. *Proc. Natl. Acad. Sci. USA* **94,** 6185-6190 (1997).

[29] Phan, A.T. Human telomeric G-quadruplex: structures of DNA and RNA sequences. *FEBS Journal* **277,** 1107-1117 (2010).

[30] Dai, J., Carver, M. & Yang, D. Polymorphism of human telomeric quadruplex structures. *Biochimie* **90,** 1172-1183 (2008).

[31] Parkinson, G.N., Lee, M.P.H. & Neidle, S. Crystal structure of parallel quadruplexes from human telomeric DNA. *Nature* **417,** 876-880 (2002).

[32] Heddi, B. & Phan, A.T. Structure of human telomeric DNA in crowded solution. *J. Am. Chem. Soc.* **133,** 9824-9833 (2011).

[33] Xue, Y., et al. Human telomeric DNA forms parallel-stranded intramolecular G-quadruplex in K^+ solution under molecular crowding condition. *J. Am. Chem. Soc.* **129,** 11185-11191 (2007).

[34] Vorlickova, M., et al. Guanine tetraplex topology of human telomere DNA is governed by the number of (TTAGGG) repeats. *Nucleic Acids Res.* **33,** 58515860 (2005).

[35] Biffi, G., Tannahill, D., McCafferty, J. & Balasubramanian, S. Quantitative visualization of DNA G-quadruplex structures in human cells. *Nature Chem.* **5,** 182-186 (2013).

[36] Miyoshi, D., Fujimoto, T. & Sugimoto, N. Molecular crowding and hydration regulating of G-quadruplex formation. *Top. Curr. Chem.* **330,** 87-110 (2013).

[37] Mariani, P., et al. Small angle x-ray scattering analysis of Deoxyguanosine 5'-Monophosphate self-assembling in solution: Nucleation and growth of G-Quadruplexes. *J. Phys. Chem.* **113,** 7934-7944 (2009).

[38] Chandrasekhar, S. & Ranganath, G.S. Discotic liquid crystals. *Rep. Prog. Phys.* **53,** 57-84 (1990).

[39] Fontes, E., Heiney, P.A. & de Jeu, W.H. Liquid-crystalline and helical order in a discotic mesophase. *Phys. Rev. Lett.* **61,** 1202-1205 (1988).

[40] Percec, V., et al. Self-organization of supramolecular helical dendrimers into complex electronic materials. *Nature* **419,** 384-387 (2002).

[41] Tan, C., Saurabh, S., Bruchez, M., Schwartz, R. & LeDuc, P. Molecular crowding shapes gene expression in synthetic cellular nanosystems. *Nat. Nanotechnol.* **8,** 602-608 (2013).

[42] Laughlan, G., et al. The high-resolution crystal structure of a parallel-stranded guanine tetraplex. *Science* **265,** 520-524 (1994).

[43] Qiu, X., Parsegian, V.A. & Rau, D.C. Divalent counterion-induced condensation of triple-strand DNA. *Proc. Natl. Acad. Sci. USA* **107,** 2148221486 (2010).

[44] Nakata, M., et al. End-to-end stacking and liquid crystal condensation of 6-to-20 base pair DNA complexes. *Science* **318,** 1276-1279 (2007).

[45] Radhakrishnan, I. & Patel, D.J. Solution structure of a pyrimidine-purine-pyrimidine DNA triplex containing TAT, C^+GC and GTA triples. *Structure* **2,** 17-32 (1994).

[46] Thenmalarchelvi, R. & Yathindra, N. New insights into DNA triplexes. *Nucleic Acids Res.* **33,** 43-55 (2005).

[47] Rau, D.C. & Parsegian, V.A. Direct measurement of temperature-dependent solvation forces between DNA double helices. *Biophys. J.* **61,** 260-271 (1992).

[48] Vorlickova, M., et al. Circular dichroism and guanine quadruplexes. *Methods* **57,** 64-75 (2012).

[49] Morikawa, M., et al. *RSC Adv.* **3,** 25694 (2013).

[50] Qiu, X., Parsegian, V.A. & Rau, D.C. Divalent counterion-induced condensation of triple-strand DNA. *Proc. Natl. Acad. Sci. USA* **107,** 2148221486 (2010).

[51] Rupprecht, A. Preparation of oriented DNA by wet spinning. *Acta. Chem. Scand.* **20,** 494-504 (1966).

[52] Cohen, J.A., et al. A phenomenological one-parameter equation of state for osmotic pressures of PEG and other neutral flexible polymers in good solvents. *J. Phys. Chem. B* **113,** 3709-3714 (2009).

[53] Robinson, R.A. & Stokes R.H. *Electrolyte Solutions* (Butterworths, London, 1959).